

Final Technical Report

Energy Saving Melting and Revert Reduction Technology (Energy SMARRT) Task 5.6 Development of CCT Diagrams

DOE Contract No. DE-FC36-04GO14230

Project Period:
October 6, 2004 – June 30, 2011

L. S. Chumbley, Principal Investigator
515-294-7903
Chumbley@iastate.edu

Iowa State University

This work was carried out with the assistance and cooperation of:

Steel Founders Society of America
John Deere
Stainless Foundry
Howell Foundry
Spuncast
Monet Metals
American Foundry
Allegheny Ludlum
MetalTek
ANCAST
Keokuk Steel Castings
Caterpillar
Bradken

August 20, 2011

Acknowledgment

This report is based upon work supported by the U.S. Department of Energy under award No. DE-FC36-04GO14230. The author wishes to thank the Steel Founders Society of America and the member companies that contributed material and in-kind contributions to this project, without which this research could not have been conducted.

Disclaimer

Any findings, opinions, and conclusions expressed in this report are those of the author and do not necessarily reflect the views of the Department of Energy.

Proprietary Data Notice

This report does not contain any proprietary data.

Report Availability

Reports are available free via the U.S. Department of Energy (DOE) Information Bridge Website: <http://www.osti.gov/bridge>

Reports are available to DOE employees, DOE contractors, Energy Technology Data Exchange (ETDE) representatives, and Informational Nuclear Information System (INIS) representatives from the following source:

Office of Scientific and Technical Information
P.O. Box 62
Oak Ridge, TN 37831
Tel: (865) 576-8401
FAX: (865) 576-5728
E-mail: reports@osti.gov
Website: <http://www.osti.gov/contract.html>

Table of Contents

List of Acronyms.....	iv
List of Figures.....	iv
List of Tables.....	v
List of Appendices.....	v
1. Executive Summary.....	1
2. Introduction.....	4
3. Background.....	5
3.1 Literature Review.....	5
3.2 Project Goals and Objectives.....	7
3.3 Planned Approach.....	8
3.4 Qualifications and Experience.....	9
4. Results and Discussion.....	9
4.1 Published Research.....	9
4.2 Summary: Equilibrium Phase Transformation Study.....	10
4.2.1 Results: CK3MCuN.....	10
4.2.2 Results: CN3MN.....	14
4.2.3 Discussion: CK3MCuN vs. CN3MN.....	19
4.3 Summary: Short-term Non-equilibrium Phase Transformation Study.....	26
4.3.1 Results: Embrittlement of CN3MN.....	26
4.3.2 Results: TTT Determination.....	29
4.3.3 Discussion: CN3MN.....	34
5. Benefits Assessment.....	35
6. Commercialization.....	35
7. Accomplishments.....	35
8. Conclusions.....	36
8.1 Research Conclusions.....	36
8.2 General Project Conclusions.....	37
9. Recommendations.....	38
10. References.....	38
11. Appendix A.....	40

List of Acronyms

BCT	body-centered -tetragonal
CCT	Continuous-Cooling Transformation
EDS	Energy Dispersive Spectroscopy
FCC	face-centered-cubic
HCP	hexagonal-close-packed
SEM	Scanning Electron Microscope
SFSA	Steel Founders Society of America
SHT	Solution Heat Treated
TEM	Transmission Electron Microscope
TTT	Time-Temperature-Transformation
WDS	Wavelength Dispersive Spectroscopy

List of Figures

Figure 1: TTT diagram as calculated by JmatPro software for sigma-, chi- and Laves-phases in wrought alloy 654 SMO.

Figure 2: TTT diagram for grain boundary precipitation in wrought alloy 254 SMO

Figure 3: Backscattered images of CK3McuN after 850 °C for 500 hours (left) and 800 °C for 500 hours (right).

Figure 4: Experimental σ volume percents and best-fit curve for CK3McuN.

Figure 5: Experimental Laves volume percents in CK3McuN and best-fit curve.

Figure 6: Volume percents (left) and number densities (right) of σ and Laves at a) 700°C b) 800°C c) 900°C in CK3McuN.

Figure 7: BSE images of CK3McuN at a) 700°C b) 800°C c) 900°C.

Figure 8: Backscattered SEM images taken at low magnification (top) and high magnification (bottom) after 2040 hours at 700 °C (left), 800 °C (middle), and 900 °C (right).

Figure 9: Experimental σ volume percents and best-fit curve for CN3MN.

Figure 10: Experimental Laves volume percents and best-fit curve for CN3MN.

Figure 11: Volume percents (left) and number densities (right) of σ and Laves at a)700°C b)800°C c)900°C in CN3MN.

Figure 12: BSE images of CN3MN at a) 700°C b) 800°C c) 900°C.

Figure 13: Microstructure evolution of CK3McuN as time increases (gray phase: σ white phase: Laves) a) As-solution heat treated with σ near voids b) σ along interdendritic boundaries c) Laves around interdendritic σ d) Fine σ and Laves within grains at higher magnification e) Growth of intragranular σ and Laves f) Growth and coarsening of intragranular σ and dissolution of Laves.

Figure 14: Microstructure evolution of CN3MN as time increases (gray phase: σ white phase: Laves) a) As-solution heat treated structure b) σ along interdendritic boundaries and near voids c) Intragranular Laves around σ near voids d) Fine Laves in intradendritic regions and fine σ in interdendritic regions e) Growth of σ and Laves f) Growth and coarsening of σ and dissolution of Laves.

Figure 15: Molar Gibb's free energy curves at constant temperature showing the equilibrium conditions for σ and metastable Laves.

Figure 16: Molar Gibb's free energy curves at constant temperature showing the minimum concentration of σ and Laves nucleation for a system with composition C_0 .

Figure 17: Impact strength as a function of time-at-temperature for an 872° C heat treatment.

Figure 18: Polished SEM images of solution heat treated CN3MN that was subsequently heat treated at 872° C for a) 5 minutes; b) 15 minutes; c) 30 minutes; d) 1 hour. Arrows show the position of the grain boundary.

Figure 19: Correlation between drop in fracture toughness and increase of grain boundary precipitation coverage.

Figure 20: Single crystal impact samples. A: embrittled sample accidentally exposed to oxygen, room temperature test; B: solution heat treated, room temperature; C: embrittled, -40° C test; D: solution heat treated, -40° C (multiple strikes); E: A mild carbon steel sample fractured at room T for comparison.

Figure 21: Impact Strength with respect to heat treatment time at a) 593 °C, b) 648 °C, c) 704 °C, d) 760 °C, e) 816 °C, f) 843 °C, g) 871 °C, h) 899 °C, i) 927 °C, and j) 982 °C.

Figure 22: Impact strength loss at 704 °C to 982 °C.

Figure 23: Impact Strength loss at 816 °C to 982 °C.

Figure 24: Embrittlement TTT Diagram with Foundry E removed from the calculation.

List of Tables

Table I: Heat treatment matrix for equilibrium phase study.

Table II: Temperature and time matrix for short term study.

Table III Microprobe WDS results for CK3McuN after 500 hours at 900 °C.

Table IV: Free energy differences between austenite and various decomposition products and expected volume percents of Laves at 700°C as predicted by JmatPro.

Table V: Linear percentage of grain boundary coverage.

Table VI: Qualitative analysis of weight percent composition of material and brittle fracture surfaces.

List of Appendices

Appendix A - Energy Savings Benefits Analysis

1. Executive Summary

One of the most energy intensive industries in the U.S. today is in the melting and casting of steel alloys for use in our advanced technological society. While the majority of steel castings involve low or mild carbon steel for common construction materials, highly-alloyed steels constitute a critical component of many industries due to their excellent properties. However, as the amount of alloying additions increases, the problems associated with casting these materials also increases, resulting in a large waste of energy due to inefficiency and a lack of basic information concerning these often complicated alloy systems.

Superaustenitic stainless steels constitute a group of Fe-based alloys that are compositionally balanced to have a purely austenitic matrix and exhibit favorable pitting and crevice corrosion resistant properties and mechanical strength. However, intermetallic precipitates such as sigma (σ) and Laves can form during casting or exposure to high-temperature processing, which degrade the corrosion and mechanical properties of the material. Knowledge of the times and temperatures at which these detrimental phases form is imperative if a company is to efficiently produce castings of high quality in the minimum amount of time, using the lowest amount of energy possible, while producing the least amount of material waste. Anecdotal evidence from company representatives revealed that large castings frequently had to be scrapped due to either lower than expected corrosion resistance or extremely low fracture toughness. It was suspected that these poor corrosion and / or mechanical properties were directly related to the type, amount, and location of various intermetallic phases that formed during either the cooling cycle of the castings or subsequent heat treatments. However, no reliable data existed concerning either the time-temperature-transformation (TTT) diagrams or the continuous-cooling-transformation (CCT) diagrams of the super-austenitics.

The goal of this study was to accurately characterize the solid-solid phase transformations seen in cast superaustenitic stainless steels. Heat treatments were performed to understand the time and temperature ranges for intermetallic phase formations in alloys CN3MN and CK3McuN. Microstructures were characterized using scanning electron microscopy (SEM), transmission electron microscopy (TEM), and energy and wavelength dispersive spectroscopy (EDS, WDS). In this way TTT and CCT diagrams could be developed for the matrix of samples chosen.

For the initial portion of this study samples were solution heat treated (SHT) then annealed at temperatures between 700 and 900°C for times from 1 minute to 2040 hours. Short-term heat treatments (up to 500 hours) were performed by transferring the sample directly from a vertical tube furnace into a salt bath. Long-term heat treatments were performed using box furnaces. This data represented the first detailed work ever conducted on cast alloys of these compositions. In the latter part portion of the study the alloy CN3MN was selected, solution heat treated, then annealed for extremely short times (0 to 960 seconds) at temperatures in the range 590°C up to 980°C.

The results of the microstructural investigation showed that the equilibrium transformation kinetics of both CN3MN and CK3McuN are extremely sluggish. Equilibrium conditions were not reached in either alloy after 2040 hour at 700 to 900°C. The transformations occurred fastest at 900°C, indicating the maximum transformation rate could be at temperatures higher than 900°C. Two dominant intermetallic phases were seen to precipitate from the austenitic matrix, BCT- σ and HCP-Laves phases as determined by TEM. These phases formed at all temperatures studied in both alloys. High-Cr plate-like σ first formed along the interdendritic boundaries and near voids. Shortly thereafter, the needle-like Laves formed intradendritically around the σ . Laves continued to nucleate within the dendrites and σ shortly followed. A high degree of macrosegregation of Mo was seen in CN3MN. Laves formed only in high-Mo interdendritic regions, while higher σ amounts were found in the intradendritic regions than in interdendritic regions. The metastable Laves phase started to dissolve shortly after reaching a maximum transformation amount, which was never more than 10 vol. %. The stable σ phase continued to grow at the maximum heat treatment time of 2040 hours at all temperatures in CN3MN and at 700 and 800°C in CK3McuN. The σ at 900°C in CK3McuN stabilized at approximately 12 vol. %.

The nucleation and growth rate of σ was much slower than the Laves, possibly due to a crystallographic orientation relationship between the HCP-Laves and FCC-austenite. The nucleation and growth rate of Laves in CN3MN was much faster at 800 and 900°C than in CK3McuN. The nucleation rate of σ was also much faster in CN3MN; however, the growth rate was slower. The slow growth rate can be attributed to the segregation of Mo in the interdendritic regions, which made the formation of Laves preferential. Once the Laves dissolved, the Cr and Mo had a much longer distance to diffuse to the σ than in CK3McuN. The macrosegregation of Mo seen in CN3MN could have been avoided if the as-cast bars were solution heat treated at temperatures and times that allowed for complete dissolution of Mo.

Number density calculations showed a maximum amount of σ precipitation and then an obvious drop off, indicating coarsening was occurring. However, the volume percents were still increasing for the same times where coarsening was observed. This indicated that growth and coarsening of σ were occurring simultaneously. This phenomenon is assumed to be a result of local compositional differences. Such measurements were not possible due to the spacing between σ precipitates being too small.

The inability to reach equilibrium conditions experimentally and inaccurate *Thermo-Calc* databases made the determination of completely accurate TTT diagrams impossible, as the values of n and k in the Avrami equation depend on the equilibrium volume percents at each isothermal temperature. It would be possible to reach equilibrium conditions if there was time to perform heat treatments for times longer than 2040 hours and at temperatures higher than 900°C.

The extremely short term heat treatments of CN3MN showed that this alloy undergoes a rapid loss in impact strength when heat treated in the range 843 °C to 982 °C due to grain boundary precipitation of intermetallics. The loss can be as great as 30% percent of the

as-solution heat treated value for times as short as 960 seconds, with a 10% loss being seen almost immediately upon heating to these temperatures. The nose of the TTT curve begins near 899 °C. Fracture surfaces of CN3MN with low impact strength display high levels of brittle fracture and surface compositions high in Mo, indicating that formation of a Mo-rich precipitate on grain boundaries is the most likely reason for the embrittlement. Due to the small size of the precipitate it was not possible to unambiguously identify this precipitate, and funding was not provided to allow TEM examination of the samples. However, it is believed that this initial precipitate may be either the Laves phase seen in the larger term studies or possibly the chi-phase seen in previous studies in the duplex alloys. This belief is somewhat supported by the observation that data from keel bars that were found to be somewhat low in Mo had lower initial strengths but were more resistant to embrittlement than those with higher Mo additions.

As this study consisted of basic research into the development of TTT and CCT diagrams as an aid to the US steel casting industry, there is no formal commercialization plan associated with this task other than presentations and publications via the Steel Founders Society of America to their members. The author is confident that the data contained in this report can be used by steel foundries to refine their casting procedures in such a way as to reduce the amount of waste produced and energy wasted by significantly reducing or eliminating the need for remelting or recasting of material due to unwanted, premature intermetallic formation.

This development of high alloy steel CCT diagrams was predicted to result in an average energy savings of 0.05 trillion BTU's/year over a 10 year period (with full funding). With 65% of the proposed funding, current (2011) annual energy saving estimates, based on initial dissemination to the casting industry in 2011 and market penetration of 97% by 2020, is 0.14 trillion BTU's/year.

The reduction of scrap and improvement in casting yield will also result in a reduction of environmental emissions associated with the melting and pouring of the steel. The average annual estimate of CO₂ reduction per year through 2020 is 0.003 Million Metric Tons of Carbon Equivalent (MM TCE).

2. Introduction

This work consisted of a basic study into the phase transformations that exist in highly alloyed steels: the phases at which they form, the rate at which they form, the temperatures of formation, and the location of phase formation as related to the overall microstructure. Such basic knowledge is crucial when moving from a relatively uncontrolled production environment to one that is designed for maximum productivity at minimum cost in energy usage, time, and effort.

Many of the standards that currently exist in the steel casting industry have developed over time due to a combination of trial and error and anecdotal evidence concerning the efficiency (and efficacy) of particular casting methods as applied to specific alloys. While these standards may allow industry to produce quality castings the majority of the time occasions arise all too often where castings have to be scrapped and product either remelted or reworked before a final product can be produced. Equally problematic is that while quality castings may be produced there is no information concerning whether the same quality could be achieved at a lower energy input. Standards are often written to allow a wide range of processes to be included since it is impossible to account for all of the individual variations that may occur as each company produces their own proprietary alloy. By providing basic information concerning phase transformations and how they are influenced by alloying elements, each company can better tailor their own individual process to take advantage of potential energy and time savings.

Many of the current problems associated with casting these alloys can be solved if better information exists concerning the phase transformations. This project was focused on acquiring just such information. Rather than create a new product or process, this project seeks to have an immediate and lasting impact on energy efficiency in the US by providing data that can be instantly implemented into existing processes. The data determined in this study will not only result in energy savings but will also serve to increase the competitiveness of the US steel casting industry by reducing costs and production times. Related gains will also be achieved in reducing harmful green-house gas emissions through elimination of wasteful re-work and/or scrapped parts.

As this study is more basic in nature and involves data collection there is no formal commercialization plan per se. However, dissemination of the results will be made to the US steel casting industry through presentations, discussions with advisory groups drawn from the industry and technical societies associated with steel casting such as the Steel Founders Society of America (SFSA), and publication of data in trade and refereed journals. Wide-spread dissemination will allow industries to incorporate the data into their existing operation plans. By careful analysis of the data individual companies can determine what changes are most suitable for their particular operations in a rapid and efficient manner.

3. Background

3.1 Literature Review:

Superaustenitic stainless steels are a group of Fe-based alloys that exhibit favorable pitting and crevice corrosion resistant properties and mechanical strength. These alloys are especially designed for highly corrosive environments at elevated temperatures. [1-5] The favorable corrosion resistant properties are attributed to the high alloy content of Cr, Mo, and N, which produce a high pitting resistance equivalent number (PREN), where:

$$(\text{PREN}) = \% \text{Cr} + 3.3 \times \% \text{Mo} + 17 \times \% \text{N} \quad \text{Equation 1}$$

These alloys are also compositionally balanced with the addition of Ni to ensure that the material remains completely austenitic. ¹²

When exposed to elevated temperatures for long periods of time, large amounts of precipitates, including carbides, nitrides and intermetallic phases, can form. [1-5] The most commonly observed secondary phases include $M_{23}C_6$ carbide, and intermetallic sigma, chi, and Laves phases. [1-5] Other less common secondary phases found in some superaustenitic alloys include M_6C , π , R and Cr_2N . [1-5] High amounts of these phases degrade the corrosion resistance and mechanical properties of the stainless steel.

There has been a large amount of research on the mechanical and corrosion resistant properties of superaustenitic stainless steels. [1-2,4-5] However, little work has been done on determining the transformation kinetics of the matrix to secondary phases as a function of time and temperature, and what has been done relates predominantly to wrought alloys. [3] Differences in the phase transformation kinetics between cast and wrought alloys, which are presumably due to differences in the nominal composition, have been documented. [6] The focus of this study is to examine the transformation behavior of cast superaustenitic steels, particularly in regards to the formation of σ and Laves phases, since they appear to be the most abundant and most detrimental to mechanical properties and corrosion resistance. [6]

As mentioned above, there have only been a few studies done on the transformation of superaustenitic stainless steels, and all of them were done on wrought alloys. Transformations of wrought alloys 254 SMO and 654 SMO were studied by Svoboda et al. [3]. It was reported that the σ , Laves, and π phases were present at 700°C up to 6170 hours. The study used the thermodynamic Calphad [7] method to calculate phase equilibrium coupled with growth kinetics modeling software, JmatPro, to calculate TTT diagrams for 5% transformation of σ -, χ - and Laves-phases for 654 SMO (Fe-24.4Cr-22Ni-7.3Mo-3.65Mn-0.5N), as presented in Figure 1. [3] A nucleation mechanism was neglected in this case. Kovach et al. [8] also reported on the 254 SMO alloy (Fe-19.9Cr-17.6Ni-6.1Mo-0.5Mn-0.2N) and a TTT diagram on the total precipitation along the grain boundaries from this experiment is presented in Figure 2. Details concerning the rate of transformations or type of precipitation were not mentioned.

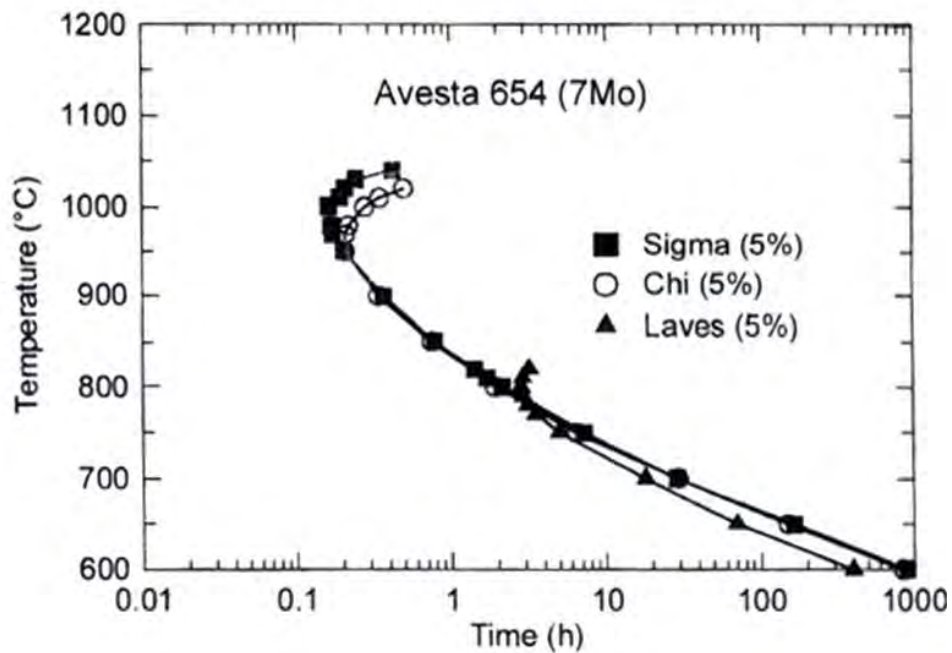


Figure 13: TTT diagram as calculated by JmatPro software for sigma-, chi- and Laves-phases in wrought alloy 654 SMO [3]

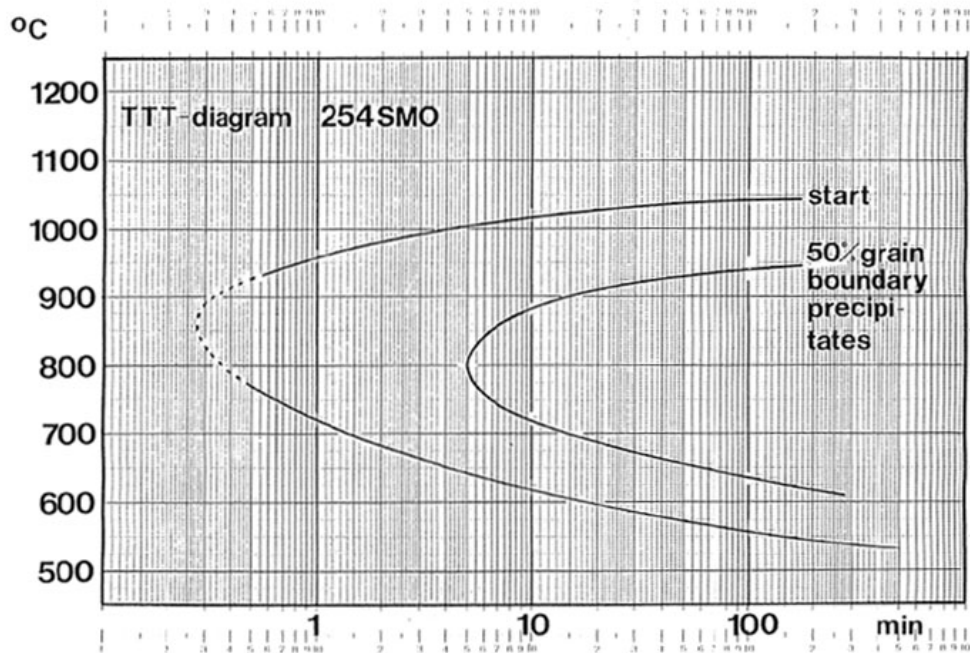


Figure 2: TTT diagram for grain boundary precipitation in wrought alloy 254 SMO [8].

Ensuring superaustenitic stainless steels maintain their optimum strength and corrosion resistance during processing and service life is essential. Previous phase transformation studies have shown that precipitate phases are slow to obtain significant volume fractions [9]. For example, the Duplex and superaustenitic stainless steels show a significant growth of precipitates (> 5 vol%) only after extended exposure to elevated temperatures [5, 10-11]. Several studies have suggested that mechanical properties such as tensile strength and hardness are not adversely affected until at least 5 vol% of precipitates is present in the matrix [5, 10-11]. Despite these results, improper heat-treatments have been shown to cause a reduction in impact strength in extremely short time periods. Several studies have suggested intermetallic phase formation is the cause [1, 12, 13], although examination of the microstructure [12] reveals that minuscule amounts (< 1 vol%) of precipitation can be detected with impact strength testing, far below the 5 vol% level.

One possible reason for the rapid embrittlement seen in highly alloyed steels is an inadequate initial solution heat treatment. Studies by Dupont [14] have shown that extended times at high temperatures are necessary to dissolve unwanted phases in to the bulk material. In some cases where the amount of Mo additions are high, which is common for many superaustenitic stainless steels, studies have found that currently specified heat treatments may fail to adequately distribute the Mo [14-16].

3.2 Project Goals and Objectives:

This study seeks to determine the isothermal transformation kinetics for cast superaustenitic stainless steel alloys CK3McuN and CN3MN. This analysis depends on extensive heat treatments followed by a complete characterization of the samples with optical microscopy and backscattered scanning and transmission electron microscopies. The transformation behavior will be further analyzed by determining volume percents and number densities of intermetallic phases as a function of heat treatment time and temperature. These analyses will be used to aid the understanding of the times and temperatures required for various phase transformations and equilibrium conditions. There has been a large amount of research on the mechanical and corrosion resistant properties of superaustenitic stainless steels. However, little work has been done on determining the transformation kinetics of the matrix to secondary phases as a function of time and temperature, and what has been done relates predominantly to wrought alloys. The results generated from this study will serve as a means to understand and control the role of various phase transformations during the production of superaustenitic stainless steel castings. A main objective of this study was to determine the loss of impact strength as a function of both time and temperature in the alloy CN3MN. Impact strength has been shown to be a very sensitive means by which embrittlement and precipitation formation can be detected. Observation of the resultant data was used to construct a time-temperature transformation (TTT) diagram for CN3MN that is applicable at extremely short time heat treatments.

3.3 Planned Approach:

The transformation kinetics and phase constituents that occur due to isothermal holds and quenching were analyzed with optical and scanning electron microscopy techniques in order to determine phase percentages. An extensive matrix of times and temperatures was used, as shown in Table I. Transmission electron microscopy was employed to identify stable phases present after extensive heat treatments. Number densities were also determined for all heat treatments to further understand the phase transformations of sigma and Laves. *Thermo-Calc*, a thermodynamic software program which uses appropriate thermodynamic databases to determine such things as driving force and equilibrium phase percentages and compositions, was used to try to predict equilibrium conditions.

Table III: Heat treatment matrix for equilibrium phase study.

	700°C	750°C	800°C	850°C	900°C
1 m	x	x	x	x	x
10 m	x	x	x	x	x
30 m	x	x	x	x	x
1 hr	x	x	x	x	x
10 hr	x	x	x	x	x
100 hr	x	x	x	x	x
500 hr	x	x	x	x	x
1000 hr	x		x		x
1500 hr	x		x		x
2040 hr	x		x		x

The effect on mechanical properties after short-term heat treatment was studied using Charpy impact testing. This method was found to be effective in determining the on-set of grain boundary precipitation even when the amount of precipitate was extremely, low, much less than 1 vol%, and the size of the precipitate was so small as to be difficult to see using SEM. Table II shows the times and temperatures used in this study.

Table II: Temperature and time matrix for short term study.

Temp (°C)	982	927	899	871	843	816	760	704	648	593
Time (sec)	0	30	60	120	240	480	960			

3.4 Qualifications and Experience:

The PI of this project has 25+ years experience and expertise in microstructural characterization using SEM, TEM, and optical microscopy coupled with x-ray spectroscopic and diffraction methods. Previous to this project he was the PI for similar study on phase transformation in the duplex stainless steel systems. The project was materially assisted by the Steel Founders Society of America (SFSA) and their collective members, who provided information, support, research reports, analysis, etc. toward this project. Especially helpful was frequent meetings with the SFSA high alloy research committee, which served as advisers for this project. The collective knowledge and wisdom of members on this panel is unsurpassed in the world.

4. Results and Discussion

The complete results of this work were published and disseminated in a number of journals and symposia as the research occurred. A summary of the results achieved are included in this paper. For additional analysis and discussion of the research as it occurred, the reader is directed to the complete listing of the published work provided below.

4.1 Published Research:

N.S.L. Phillips, L.S. Chumbley, B. Gleeson, "Determination of Isothermal Diagrams for Sigma and Chi Phase Formation in Superaustenitic Stainless Steels," Technical and Operating Conference, Steel Founders Society of America, Chicago, IL, Nov 2-5, 2005.

N. Phillips, L.S. Chumbley, B. Gleeson, and O. Ugurlu "Determination of Phase Transformations in Cast Superaustenitic Stainless Steels," Technical and Operating Conference, Steel Founders Society of America, Chicago, IL, Dec 14-16, 2006.

Phase Transformations in Cast Superaustenitic Stainless Steels, Nathaniel S.L. Phillips, L. Scott Chumbley, Brian Gleeson, Master of Science thesis, Iowa State University, 2007.

C. Muller, L.S. Chumbley, "Investigation of Reduced Fracture Toughness in Superaustenitic Stainless Steels," Technical and Operating Conference, Steel Founders Society of America, Chicago, IL, Dec 12-15, 2007.

N.S.L. Phillips, L.S. Chumbley, B. Gleeson, "Phase Transformations in Cast Superaustenitic Stainless Steels," J. Mat Eng. And Perf., 18, 9, 1285-1293, 2009.

C. Muller, L. Scott Chumbley, "Fracture Toughness of Heat Treated Superaustenitic Stainless Steels," J. Mat. Eng. And Perf., 19, 5, 714-720, 2009.

B. King, S. Chumbley, "Transformation Diagram Determination using Impact Testing," Proceeding, Technical and Operating Conference, Steel Founders Society of America, Chicago, IL, December, 2010.

B.W. King, L.S. Chumbley, "Transformation Diagram Determination Using Impact Testing," accepted Int. J. Mat. Eng. Tech.

4.2 Summary: Equilibrium Phase Transformation Study

4.2.1 Results: CK3McuN

Contrast variations in backscattered electron (BSE) images made it possible to differentiate between phases due to atomic number differences. Precipitation of intermetallic phases was found after heat treatments at low temperatures (700°C) and short soak times (1 minute) in CK3McuN. Figure 3 shows examples of typical microstructures observed after long aging times. While precipitation starts along the interdendritic boundaries, growth continued both at the boundaries and homogeneously within the dendrites as heat treatment times and temperatures increased. A coarsened gray phase is first seen along the interdendritic boundaries; shortly thereafter a needle-like white phase precipitates.

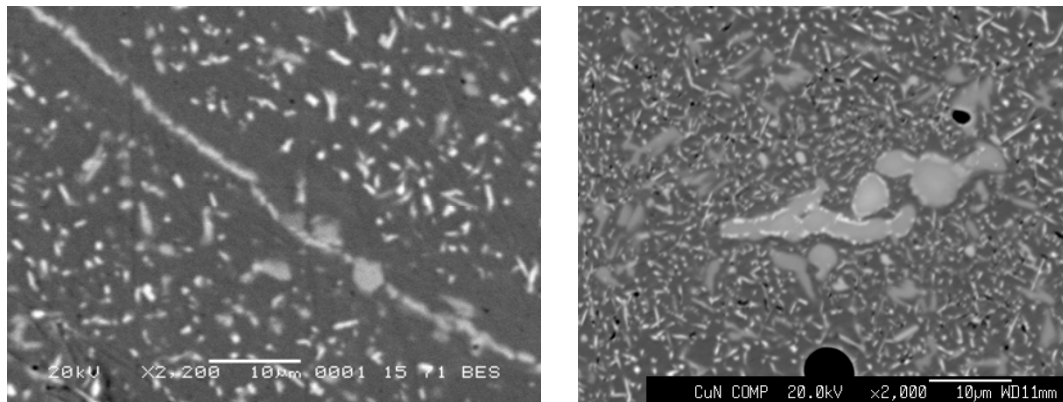


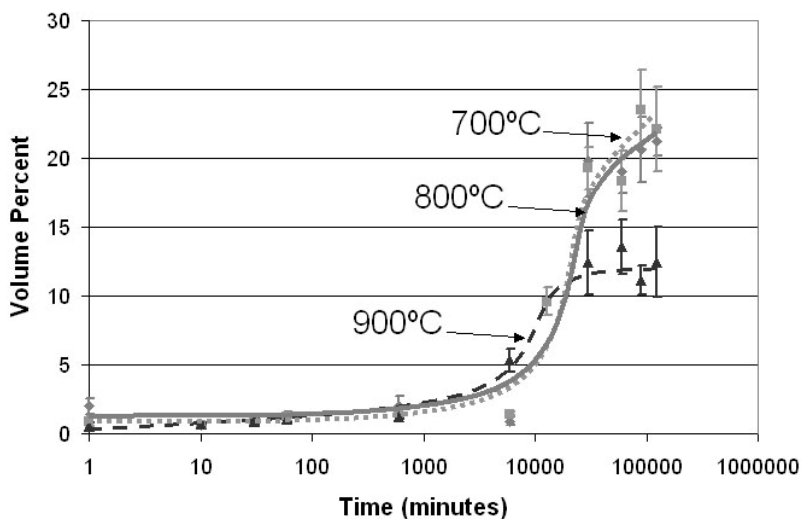
Figure 14: Backscattered images of CK3McuN after 850 °C for 500 hours (left) and 800 °C for 500 hours (right).

Results obtained from WDS scans of several white and gray precipitates seen in the 900°C, 500 hour heat treatment sample are presented in Table III. (These quantitative compositions were used in comparison to the qualitative EDS compositions obtained during initial screening of phases to be identified with TEM.) TEM analysis of a CK3McuN sample heat treated at 800°C for 500 hours confirmed that the high-Cr gray phase was σ and the high-Mo white phase was Laves.

Table IVII Microprobe WDS results for CK3McuN after 500 hours at 900 °C.

Composition (wt. %)						Phase
Si	Fe	Mo	Cr	Ni	Mn	
2.6±0.4	40.7±3.3	28.0±5.8	17.2±1.0	10.5±1.6	0.5±0.08	White
1.4±0.7	42.6±3.5	12.8±1.7	31.9±1.6	9.7±2.1	0.6±0.08	Gray
0.4±0.1	56.3±1.0	2.7±0.4	20.5±0.1	17.5±0.1	0.8±0.1	Matrix

Metallographic examination of CK3McuN samples showed a small amount of σ phase was present in the solution heat-treated samples before the isothermal hold. Nucleation of the σ phase was low until approximately 100 hours at all temperatures, after which an increase in the number of precipitates was seen. Subsequent growth occurred very slowly, such that equilibrium was not reached at 700 and 800°C even after the maximum heat treatment time of 2040 hours. Volume percents seen after this time are above 20%. The amount of σ at 900°C leveled off at ~12%. Measured σ volume percentage data with error bars of one standard deviation are presented with a best-fit curve in Figure 4.

Figure 4: Experimental σ volume percents and best-fit curve for CK3McuN.

Metallographic examination did not reveal any Laves present in the solution heat-treated structure. However, Laves was present after about 30 minutes at 900°C and 500 hours at 700 and 800°C. The Laves phase reached a maximum of 4.6, 6.8, and 10.0% at 700, 800, and 900°C, respectively, at 500 hours. The dissolution of Laves phase was apparent after 100, 250, and 500 hours at 900, 800, and 700°C, respectively. Measured Laves volume percentage data with error bars of one standard deviation are presented with best-fit curves in Figure 5.

The contrast of phases in the BSE images also made it possible to calculate the number densities of σ and Laves for all heat treatments. The volume percentages are compared to the number densities for σ and Laves at 700, 800, and 900°C in Figure 6, which are shown plotted with one standard deviation error bars. Microstructures that correspond to these graphs can be found in Figure 7.

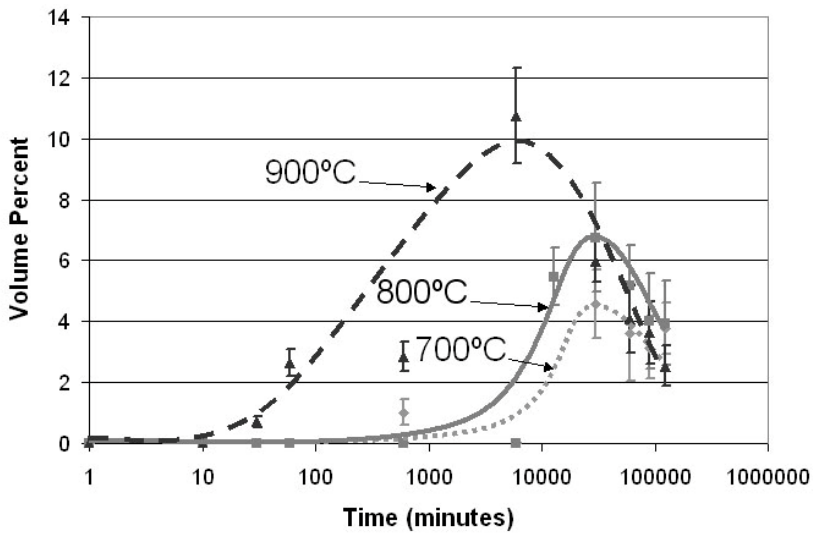
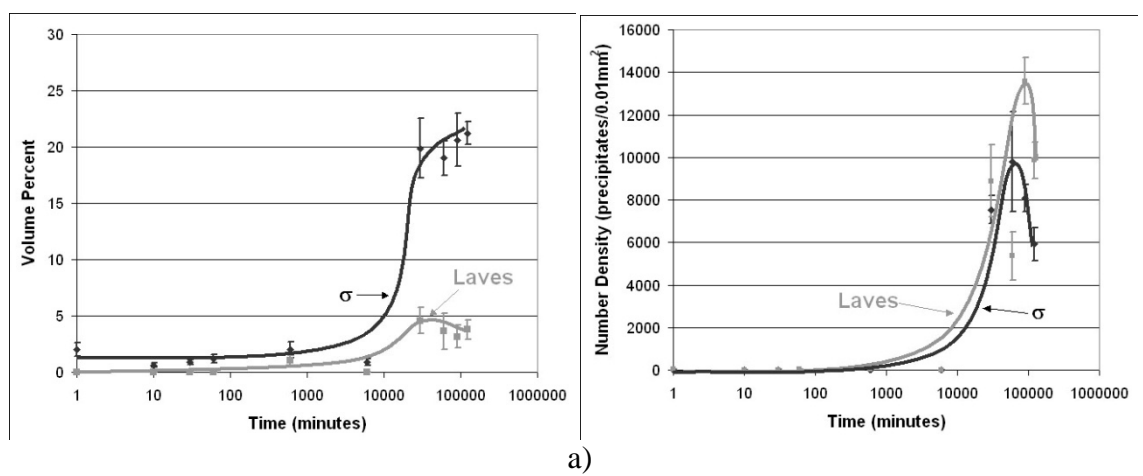


Figure 5: Experimental Laves volume percents in CK3McuN and best-fit curve.



a)

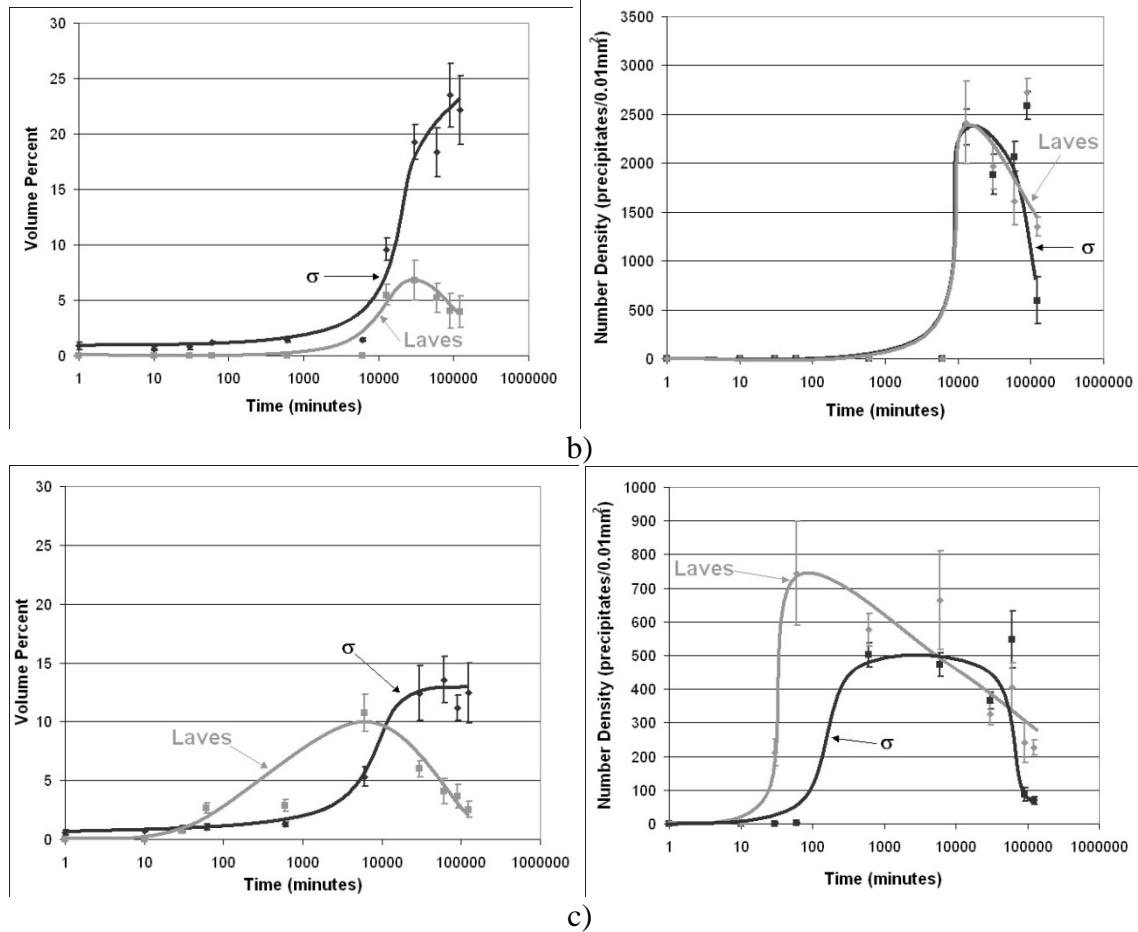
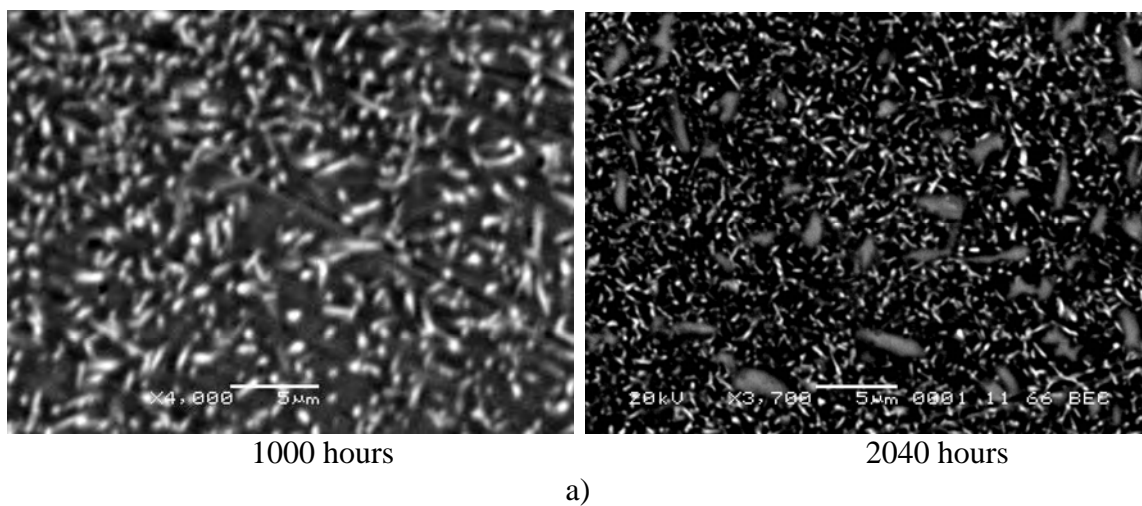


Figure 6: Volume percents (left) and number densities (right) of σ and Laves at a) 700°C b) 800°C c) 900°C in CK3McuN.



a)

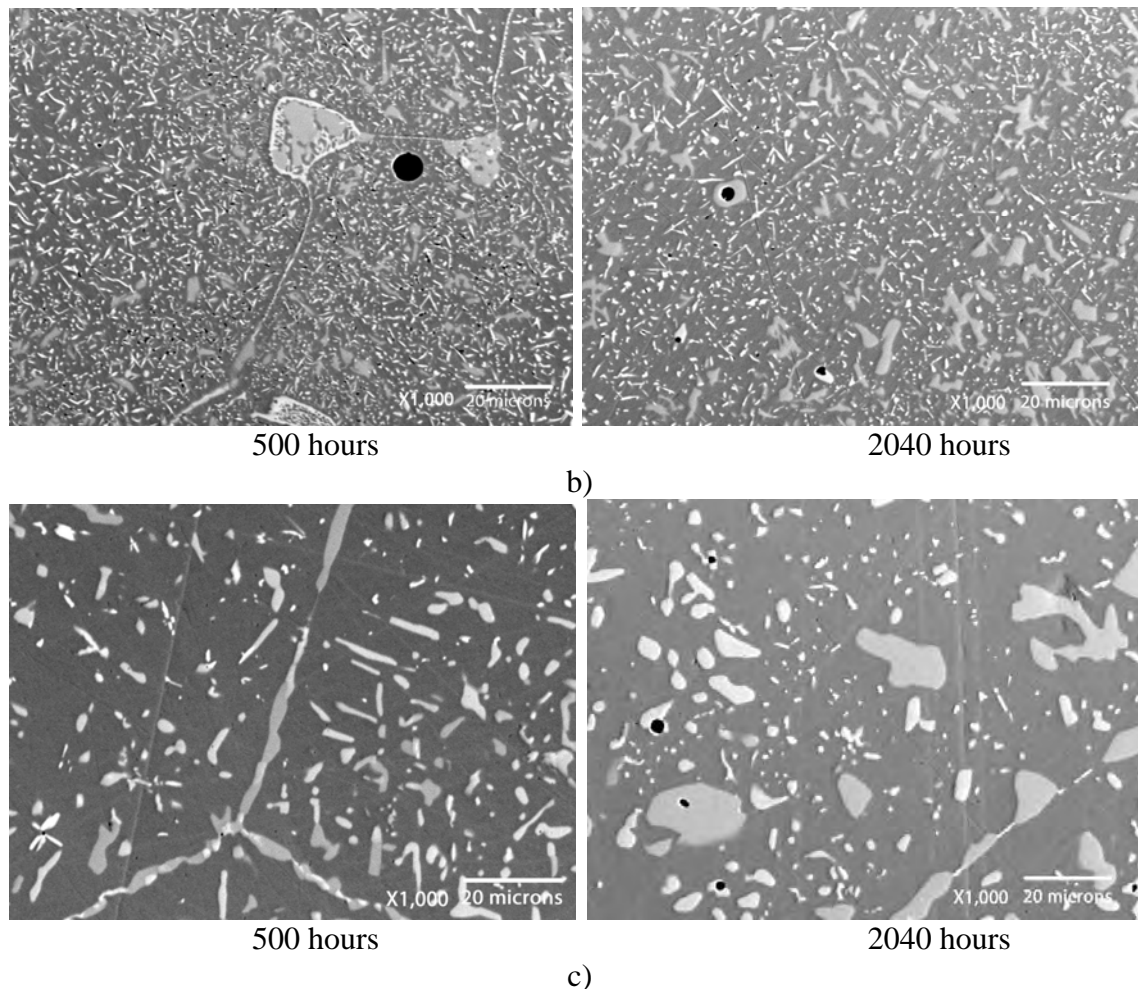


Figure 7: BSE images of CK3McuN at a) 700°C b) 800°C c) 900°C.

4.2.2 Results: CN3MN

Intermetallic phases similar to what were seen in CK3McuN were observed at similar temperatures in CN3MN. Precipitation again was observed to first form along the interdendritic boundaries, although the scale of the precipitates was much finer than that of CK3McuN for aging times up to 500 hours. Phase characterization proved to be extremely difficult in this alloy due to the fine scale of the precipitates, which was below the spatial resolution of EDS and WDS using SEM techniques for accurate chemical analysis. TEM was used again to positively identify the phases in CN3MN. Both σ and Laves were found in a sample heat treated at 800°C for 2040 hours. The lattice parameters and EDS compositions of both phases were very similar to those found for σ and Laves in CK3McuN.

Unlike CK3McuN, a significant amount of macrosegregation corresponding to the original cast dendritic structure was observed at all temperatures for all times (Figure 8). At the longest times studied it was evident that growth of σ was favored in the former intradendritic regions while Laves was favored in the interdendritic regions.

Compositional map scans using WDS revealed the macrosegregation of Mo in the solution heat-treated samples.

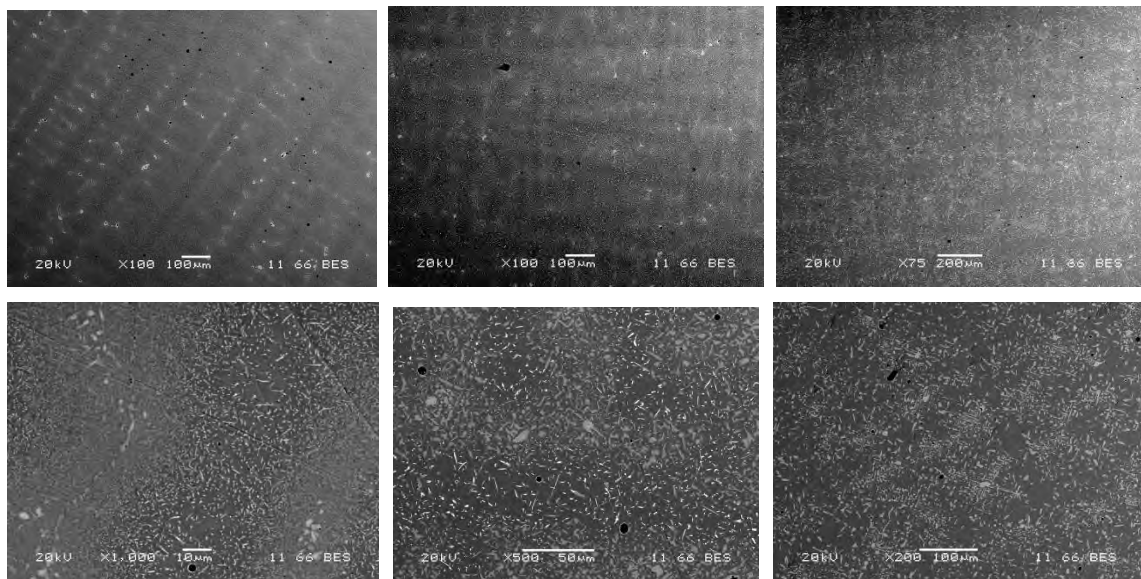


Figure 8: Backscattered SEM images taken at low magnification (top) and high magnification (bottom) after 2040 hours at 700 °C (left), 800 °C (middle), and 900 °C (right).

Metallographic examination of CN3MN showed that σ and Laves nucleated at longer times than for CK3McuN. The interdendritic region (high Mo concentration) was observed to be favorable for Laves nucleation, while the intradendritic region (low Mo concentration) favored σ nucleation. At 900°C, the microstructure seems to be completely σ for all times greater than 1000 hours. Experimental volume percentage data for σ and Laves with error bars of one standard deviation are presented with best fit-curves in Figure 9 and 10, respectively. It is apparent that the σ volume percent will continue to increase after 2040 hours at all temperatures. The Laves phase dissolved at 800 and 900°C after 1000 and 10 hours with maximum volume percents of 5.3 and 6.6%, respectively. The high amount of error associated with the volume percent measurements was a direct result of the observed macrosegregation.

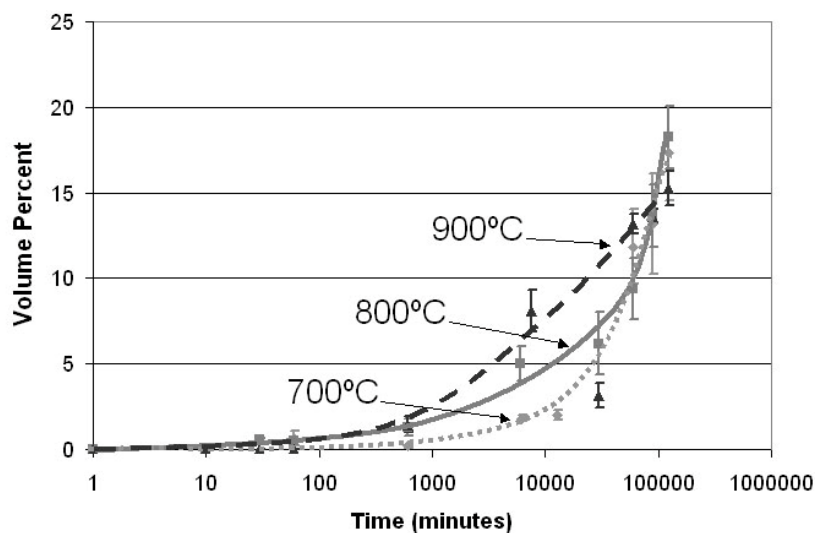


Figure 9: Experimental σ volume percents and best-fit curve for CN3MN.

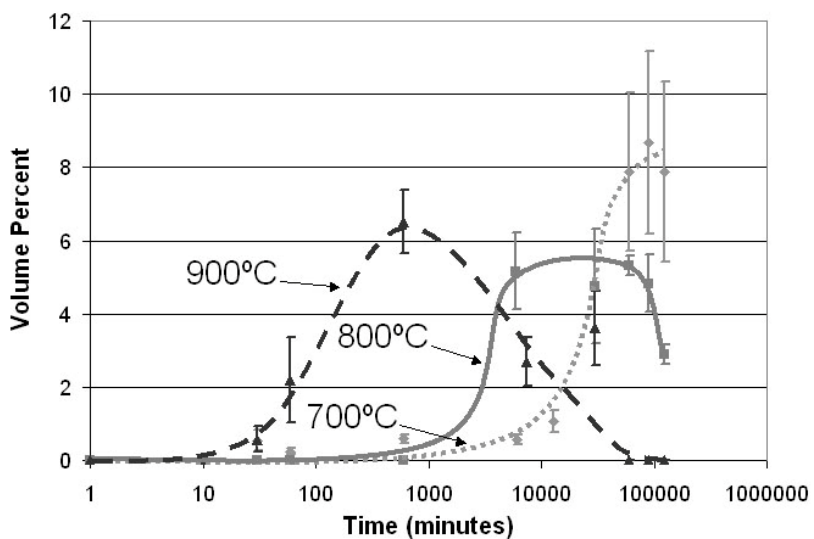


Figure 10: Experimental Laves volume percents and best-fit curve for CN3MN.

The volume percentages and number densities for σ and Laves at 700, 800, and 900°C are presented in Figure 11. Error bars are once again high due to macrosegregation and the finer size-scale of the precipitates. Microstructures that correspond to these graphs are presented in Figures 12.

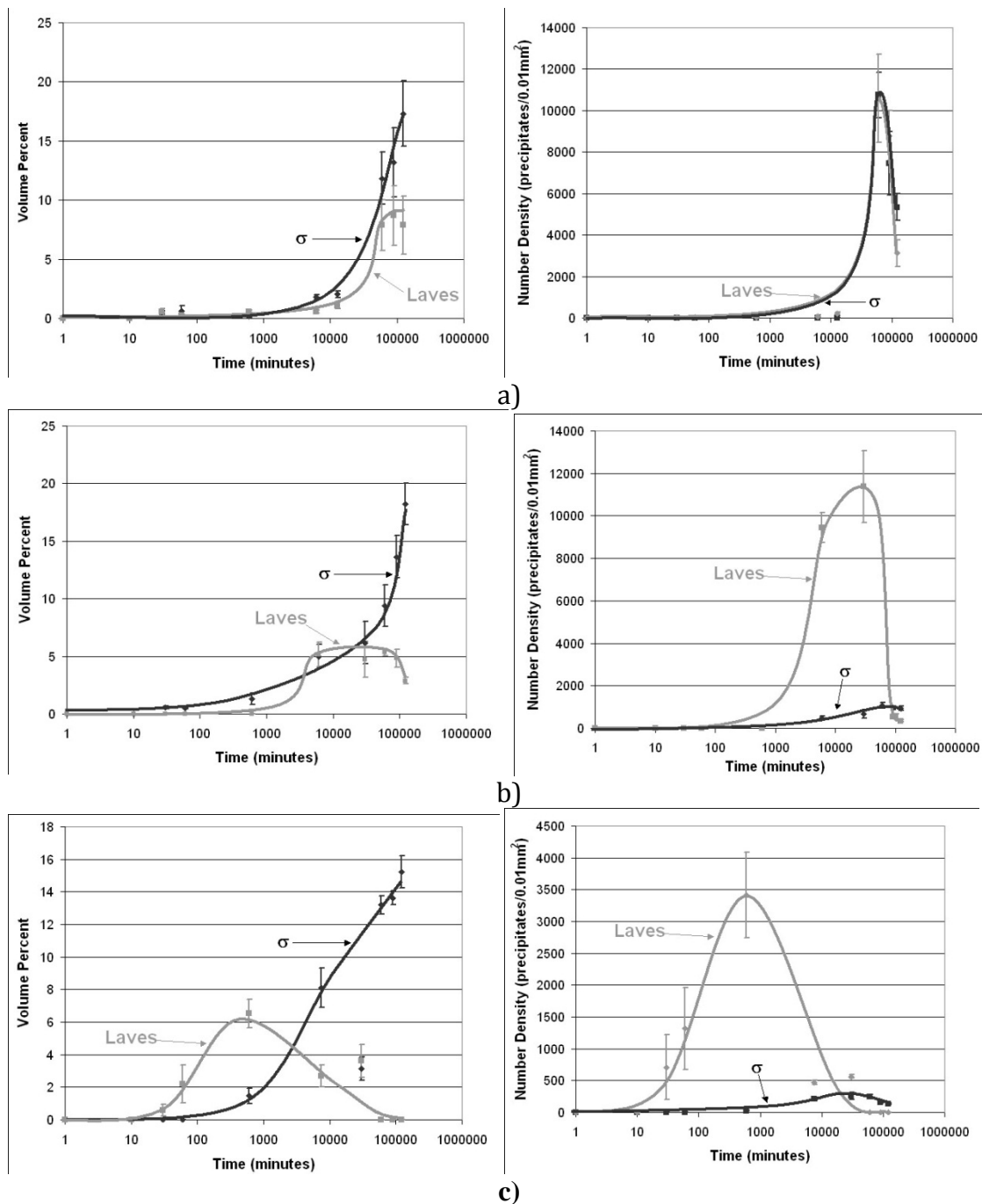


Figure 11: Volume percents (left) and number densities (right) of σ and Laves at a)700°C b)800°C c)900°C in CN3MN.

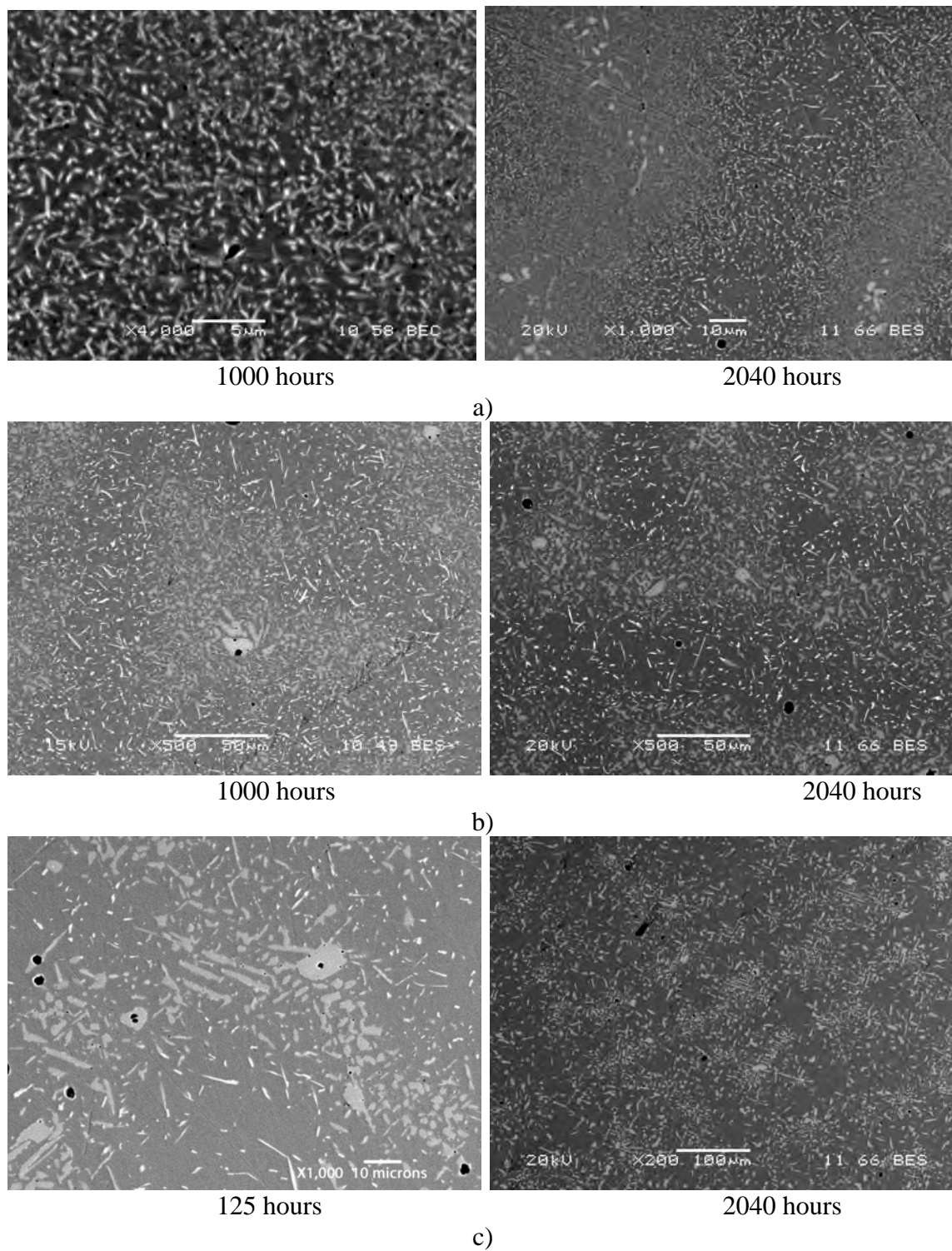


Figure 12: BSE images of CN3MN at a) 700°C b) 800°C c) 900°C.

4.2.3 Discussion – CK3McuN vs. CN3MN:

A general sequence of the phase transformations seen at all temperatures in CK3McuN and CN3MN is presented in Figures 13a-f and 14a-f, respectively. The size scale of the precipitates is not accurate for all temperatures, but gives a general understanding of how the phases nucleate, grow, and coarsen as time increases. The microstructures for both alloys showed similar behavior at short heat treatment times at all temperatures. However, due to segregation of Mo in CN3MN, the microstructures were very different for longer heat treatment times. The σ phase initially formed along interdendritic boundaries and near voids for both alloys. Larger precipitates often formed in these areas, similar to what is seen in Figure 13b. There was a small amount (<0.5 %) σ precipitation in the as-solution heat treated structure for CK3McuN; whereas, it took between 30 to 60 minutes for σ to nucleate in CN3MN. Laves formation apparently followed that of σ in the interdendritic boundaries and near voids.

Intradendritic precipitation of very fine needle-like Laves always followed Laves precipitation near the σ along the interdendritic boundaries and near voids. The Laves particles that surrounded the σ on the interdendritic boundaries were always larger than the Laves particles that nucleated within the dendrites, away from the interdendritic boundaries. Fine intradendritic σ precipitation usually followed the intradendritic precipitation of Laves. These former precipitates were more spherical than the intradendritic Laves. Similar to Laves, the intradendritic σ precipitates were much smaller in size compared to the σ found along the interdendritic boundaries and near voids. This was why the average size of the particles was very high for short times and dropped off as σ and Laves started to nucleate within the grains. Once growth and coarsening of both phases commenced, the average size also started to increase. In CN3MN, Laves was only seen in the interdendritic regions, where the high amounts of Mo segregation occurred. The intradendritic σ that nucleated in this alloy was in greater amount than in the interdendritic regions. At longer times (≥ 500 hours), Laves was seen to nucleate on the σ throughout both alloys.

The maximum size of Laves particles was much larger in CK3McuN than in CN3MN at all temperatures. The Laves precipitates in CK3McuN became more spherical as time progressed, while they remained needle-like at all times in CN3MN. After the Laves reached a certain maximum amount, it started to dissolve back into solution. This was evident at all temperatures for CK3McuN and at 800 and 900°C in CN3MN. Laves dissolved completely at 900°C for CN3MN. The maximum size of a Laves precipitate before it dissolved was never as large as the σ precipitation for the same time and temperature.

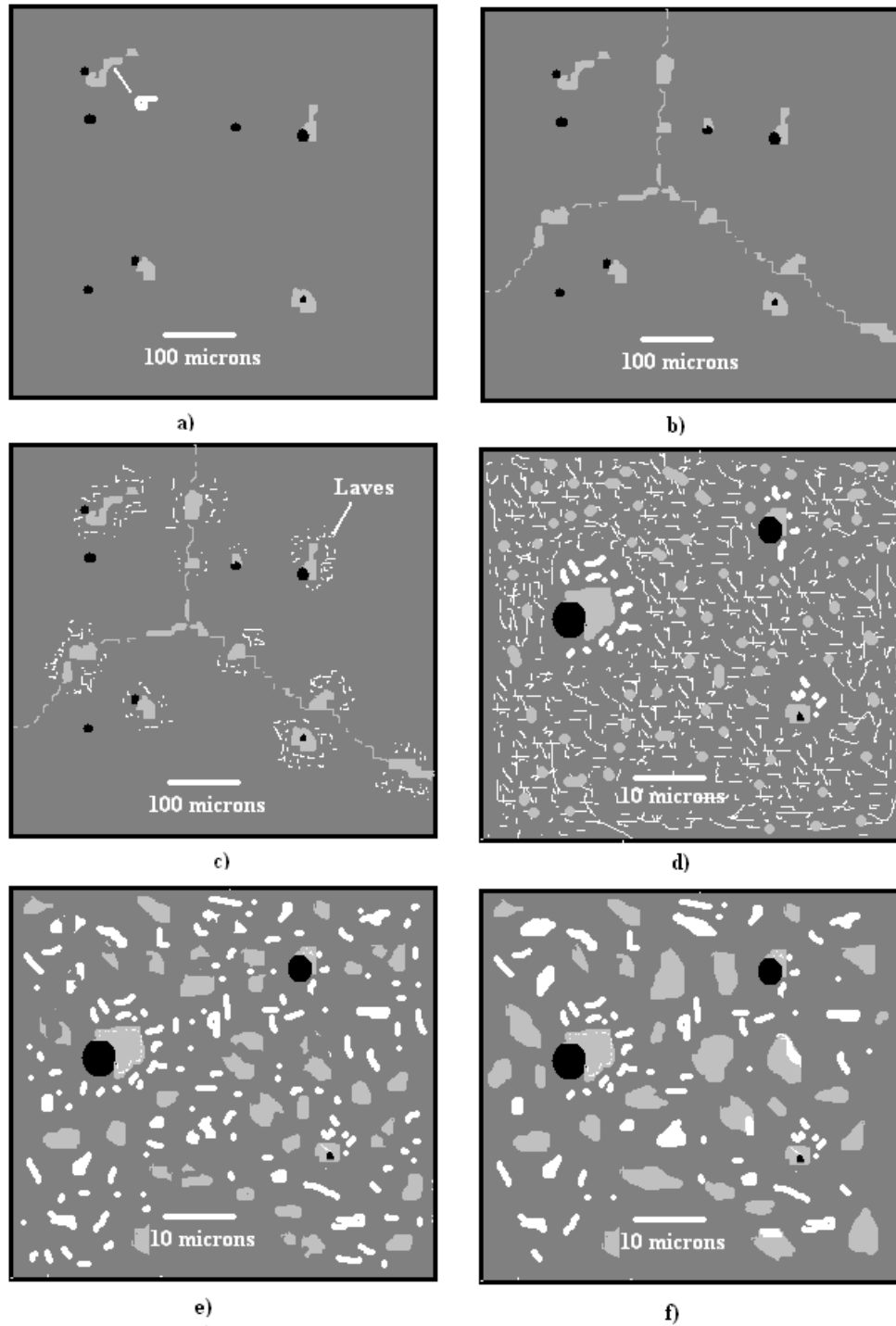


Figure 13: Microstructure evolution of CK3McuN as time increases (gray phase: σ white phase: Laves) a) As-solution heat treated with σ near voids b) σ along interdendritic boundaries c) Laves around interdendritic σ d) Fine σ and Laves within grains at higher magnification e) Growth of intragranular σ and Laves f) Growth and coarsening of intragranular σ and dissolution of Laves.

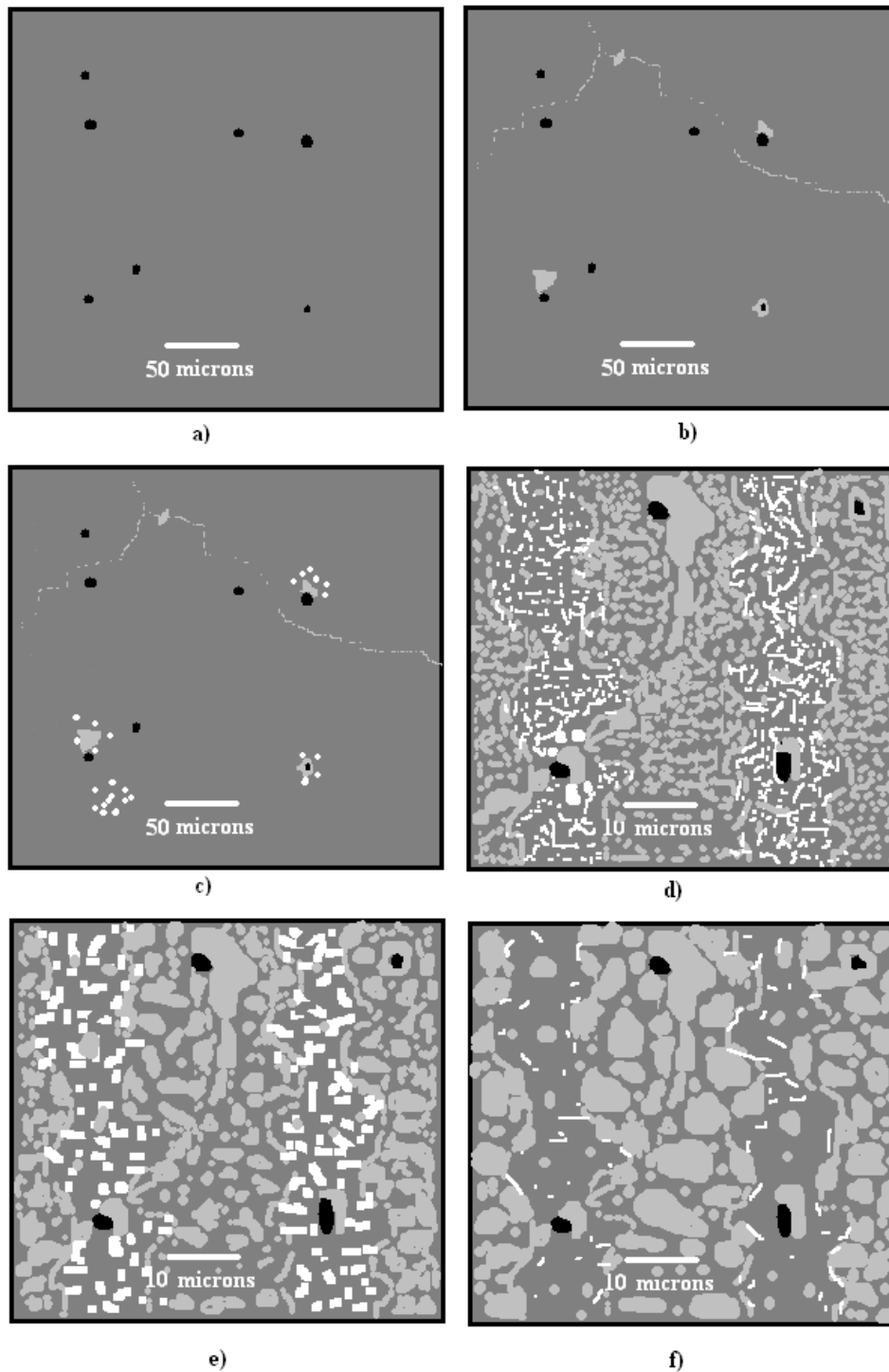


Figure 14: Microstructure evolution of CN3MN as time increases (gray phase: σ white phase: Laves) a) As-solution heat treated structure b) σ along interdentritic boundaries and near voids c) Intragranular Laves around σ near voids d) Fine Laves in intradentritic regions and fine σ in interdentritic regions e) Growth of σ and Laves f) Growth and coarsening of σ and dissolution of Laves.

Differentiation between σ and Laves based on contrast using backscattered electrons was more uncertain for samples aged at intermediate times and lower temperatures since small Laves precipitates that might normally appear white due to atomic number contrast could appear gray due to beam spreading effects. Thus, the errors associated with the calculation of volume percents, number densities, and average particle sizes were greater for the heat treatments where the contrast was not as high (i.e. intermediate times and lower temperatures).

The volume percent determinations revealed that the time needed to start nucleating σ along the interdendritic boundaries is much shorter in CK3McuN than in CN3MN. However, the overall time required to nucleate σ intragranularly before it started to grow appeared to be shorter in CN3MN than CK3McuN. Growth started after 10 hours at all temperatures in CN3MN. Similarly, growth started after 10 hours at 900°C in CK3McuN, but did not start until after 100 hours at 700 and 800°C. The rates at which σ grew in the two alloys were vastly different. In CK3McuN, the σ volume percents apparently started to reach equilibrium at 900°C after about 500 hours; whereas, the volume percents are still growing at 700 and 800°C up to the maximum heat treatment time of 2040 hours. The σ volume percents in CN3MN were still increasing at a steady rate up to 2040 hours at all temperatures.

The time needed to nucleate Laves was similar at 700 and 900°C in both alloys. However, at 800°C the time needed to nucleate Laves was much longer in CK3McuN. The time required to reach maximum growth at 900°C in CK3McuN is much longer than in CN3MN, while the times were quite similar for both alloys at 800°C. However, Laves was still growing at 2040 hours at 700°C in CN3MN. An obvious dissolution of Laves occurred at all temperatures in CK3McuN, while dissolution was only seen at 800 and 900°C in CN3MN.

The number densities of both σ and Laves as a function of time for CK3McuN of both σ and Laves reached a maximum, which would indicate the end of nucleation and the beginning of growth. For 700 and 800°C, the number densities reached a maximum and then decreased due, in part, to the start of coarsening of both phases. The number of Laves precipitates would also decrease as dissolution occurred. At 900°C, a similar maximum was seen for Laves; however, the growth of σ occurred over a range of times before starting to coarsen.

The number densities for CN3MN reveal that the number of Laves precipitates decreased at all temperatures, including 700°C, as time increased. The overall number of σ precipitates was much lower than the number of Laves precipitates at 800 and 900°C before dissolution occurs, even though the volume percents of σ were higher for the same times. Thus, the average size of a Laves particle was much smaller than the average size of a σ particle at all times. The number density of σ also appeared to increase at the same time the number density of Laves decreased at 800 and 900°C. This would suggest that σ nucleation was a direct result of the Laves dissolution.

Nucleation rate is dependent on how fast critical- sized nuclei can receive an atom from the matrix and on the concentration of critical sized nuclei. How fast an atom is received from the matrix is determined by the rate of diffusion and the surface area of the critically-sized nucleus. The critical nucleus size needed for nucleation requires a small surface energy and/or a large driving force. The barrier to nucleation, ΔG^* , is proportional to (γ^3/G_v^2) . As the driving force increases and the surface energy decreases, the nucleation rate will increase, as given by the equation:

$$N_{\text{het}} = \omega C_1 \exp(-\Delta G^*/kT) \exp(-\Delta G_m/kT) \quad \text{Equation 2}$$

where N is the rate for heterogeneous nucleation, C_1 is the concentration of heterogeneous nucleation sites, ω is a factor that includes the vibration frequency of the atoms and the area of the critical nucleus, ΔG_m is the activation energy for atomic migration, k is Boltzman's constant and T is temperature.

Based on the results presented, an inferred set of Gibb's molar free energy curves as a function of composition for the stable phases γ and σ and metastable Laves are presented in Figure 15. The composition of γ in equilibrium with Laves and σ is given by C_L and C_{eq} , respectively. It was observed that σ nucleated first in both CK3McuN and CN3MN along the interdendritic boundaries and near voids at all temperatures. Under these conditions, the γ -matrix is at some supersaturated composition C_o . Figure 16 shows that for a matrix at C_o , the minimum nuclei composition for Laves and σ would be C_1 and C_2 , respectively, since it is at these compositions that the σ and Laves would first have negative driving forces for formation. This would suggest that the metastable Laves could form first, because the diffusion needed to reach C_1 is less than the diffusion needed reach C_2 . However, the interdendritic boundaries provide paths for rapid diffusion compared to intradendritic regions, so that the former sites would favor the nucleation of the stable σ .

The local concentration of vacancies is expected to be higher in the vicinity of a heterogeneous site, such as a grain boundary, than in a homogeneous site. Moreover, the diffusion coefficient for a substitutionally diffusing metal atom will be greater where the concentration of vacancies is higher. Therefore, as the concentration of vacancies increases, the rate of diffusion increases. The concentration gradient between the matrix and a heterogeneous site is also much higher than between the matrix and homogenous nucleation site, causing the overall flux of atoms to be greater for areas such as interdendritic boundaries and voids. Therefore, the diffusion rate of metal atoms would be faster in the vicinity of interdendritic boundaries and voids than in intradendritic regions. The faster rate of diffusion would cause the system to form the stable σ phase along the interdendritic boundaries or near voids before metastable Laves forms intragranularly around the σ .

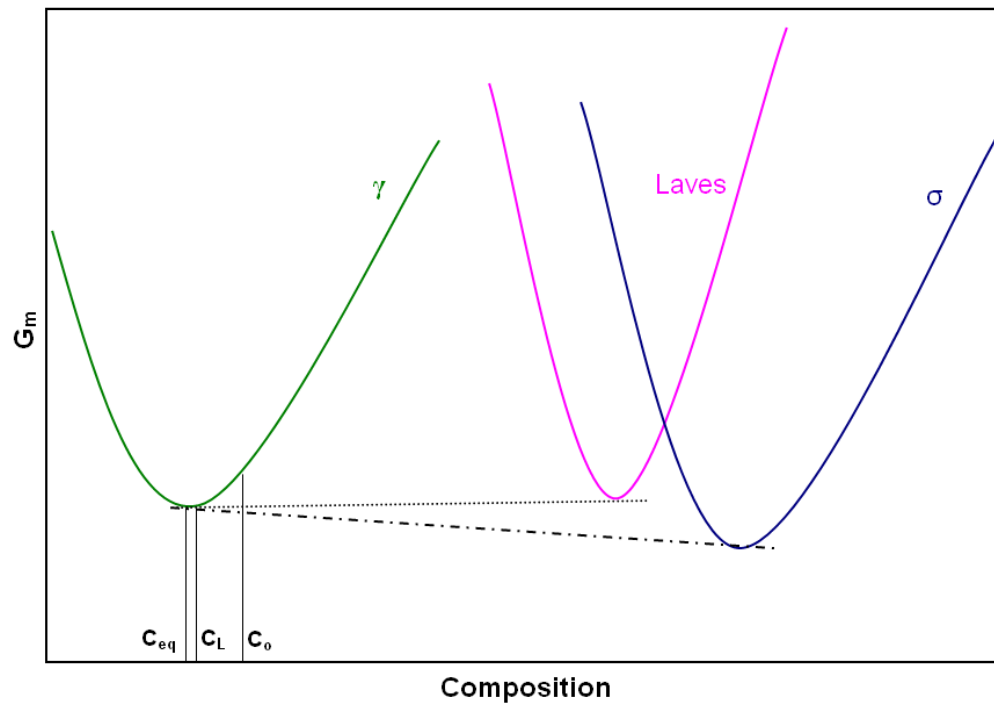


Figure 15: Molar Gibb's free energy curves at constant temperature showing the equilibrium conditions for σ and metastable Laves.

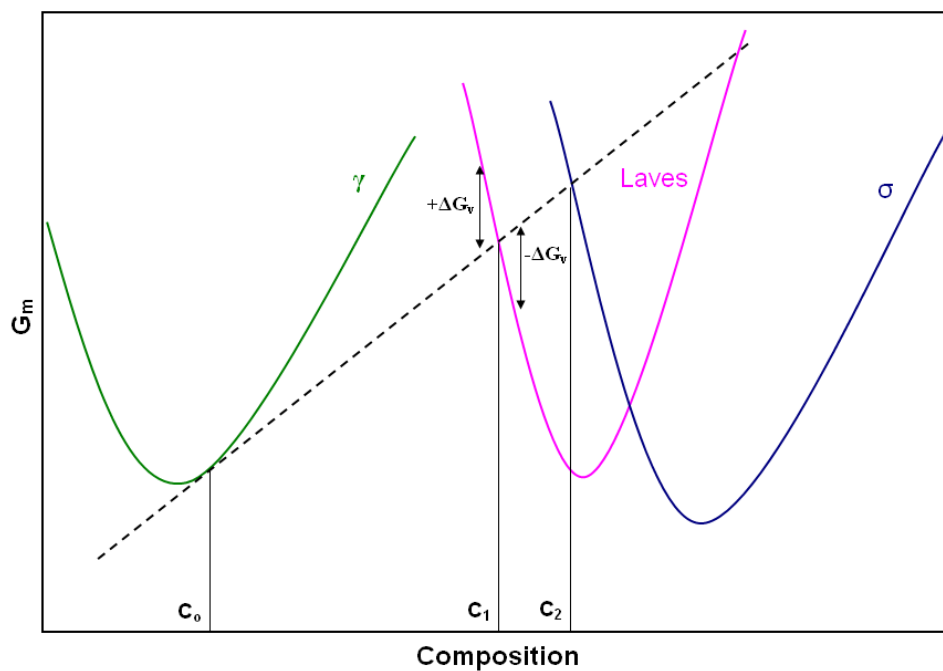


Figure 16: Molar Gibb's free energy curves at constant temperature showing the minimum concentration of σ and Laves nucleation for a system with composition C_0 .

Next, much finer Laves nucleates intradendritic in regions away from the interdendritic boundaries and voids. Intradendritic σ nucleates after Laves in similar regions. While the driving forces of σ and Laves may be only slightly different, the nucleation rate of the Laves phase appears to be equally as fast or faster than σ at all temperatures for both alloys. This is believed to be a result of the interfacial energy between the matrix and precipitate nuclei being less for the γ /Laves interface than the γ / σ interface. The interfacial energy between FCC- γ and HCP-Laves is assumed to be much lower than between FCC- γ and BCT- σ , since FCC and HCP are both closed-packed crystallographic structures. The (0001) and (111) are both closed pack planes with atomic packing factors of 0.74.

Svoboda et al.³ also attributed the earlier formation of Laves to a suspected orientation relationship between γ and Laves. These authors reported on the free energy differences between austenite and various decomposition products for the wrought alloy Avesta 654 (Fe-24.4Cr-21.9Ni-7.3Mo-3.65Mn-0.5N) at 700°C, as predicted by the thermodynamic and kinetic program, JmatPro. As shown in Table IV, the free energy difference for the formation of austenite + Laves is slightly less than the free energy difference for the formation of austenite + Laves + σ . The expected volume percents at 700°C are also predicted for the same decompositions. The expected volume percents of Laves at 700°C match well with the experimental results for Laves in CN3MN.

Table IV: Free energy differences between austenite and various decomposition products and expected volume percents of Laves at 700°C as predicted by JmatPro [3]

Decomposition Reaction	ΔG , J/mol	Expected vol. % of Laves
$\gamma \rightarrow \gamma + \text{Laves}$	-148	12%
$\gamma \rightarrow \gamma + \text{Laves} + \sigma$	-223	8-10%

Since both σ and Laves are rich in Cr and Mo, they were competitively growing against one another. The growth rates of σ and Laves depend on the diffusion of Mo and Cr through the γ matrix and the surface energy associated with each precipitate. The maximum size of a Laves precipitate before it dissolves was never as large as the maximum size of a σ precipitate. Since Laves is high in Mo, it can be assumed that the diffusion of Mo was very slow in Laves formation. The Laves phase, as mentioned previously, was energetically favored to nucleate intragranularly first due to lower interfacial energy between the matrix and Laves nuclei. The formation of Laves would decrease the availability of Cr and Mo for σ formation and growth, in the early stages. However after σ nucleates and starts to grow, the average size of the spherical-like σ particles are much larger than the needle-like Laves particles.

The dissolution of Laves after it reached a maximum amount led to further growth of σ . The equilibrium driving force of σ is larger than the metastable equilibrium driving force of Laves, as shown in Figure 15, which causes the system to favor the formation of σ . The number densities of σ started to increase at higher rates as the Laves started to

dissolve, as seen at higher temperatures. Therefore, local composition differences would occur in areas where σ is at equilibrium, causing it to coarsen, and areas where it is growing, due to the dissolution of Laves.

The dependence of σ formation on Laves dissolution in CN3MN can also be described by such a phenomenon. As the system approaches equilibrium, the Cr and Mo would have much further to diffuse to the σ in the intradendritic regions than if the Laves and σ were growing together in the same regions, as seen in CK3McuN. This explains why the growth of the σ is much slower in CN3MN than CK3McuN. This would also explain the local composition differences causing growth and coarsening to occur simultaneously.

4.3 Summary: Short-term Non-equilibrium Phase Transformation Study

4.3.1 Results: Embrittlement of CN3M

Initial attempts used full-sized Charpy impact specimens of polycrystalline CN3MN to test embrittlement as a function of heat treatment temperature. Standard-sized specimens withstood the full 300 ft-lb force applied in the fully SHT condition. Rapid embrittlement was seen in samples heat treated at 872° C, as shown in Figure 17.

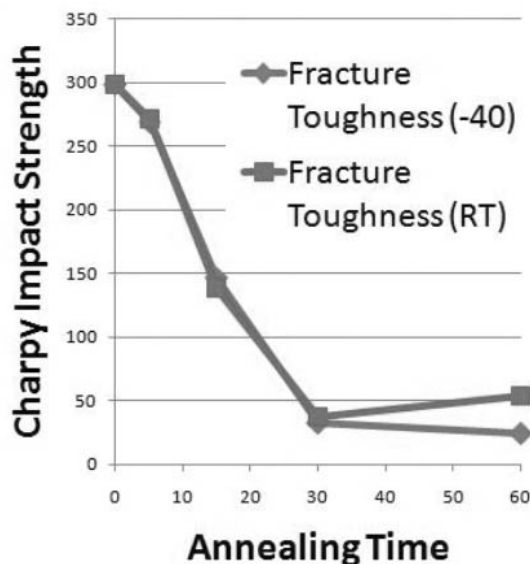


Figure 17: Impact strength as a function of time-at-temperature for an 872° C heat treatment.

SEM micrographs of polished samples corresponding to samples heat treated at 872° C are shown in Figure 18. It is difficult to determine in the earliest stages (5 and 15 minutes) whether precipitation is present on the grain boundary as a thin layer. Some discrete particles appear to be forming after 15 minutes and can clearly be resolved after 30 minutes.

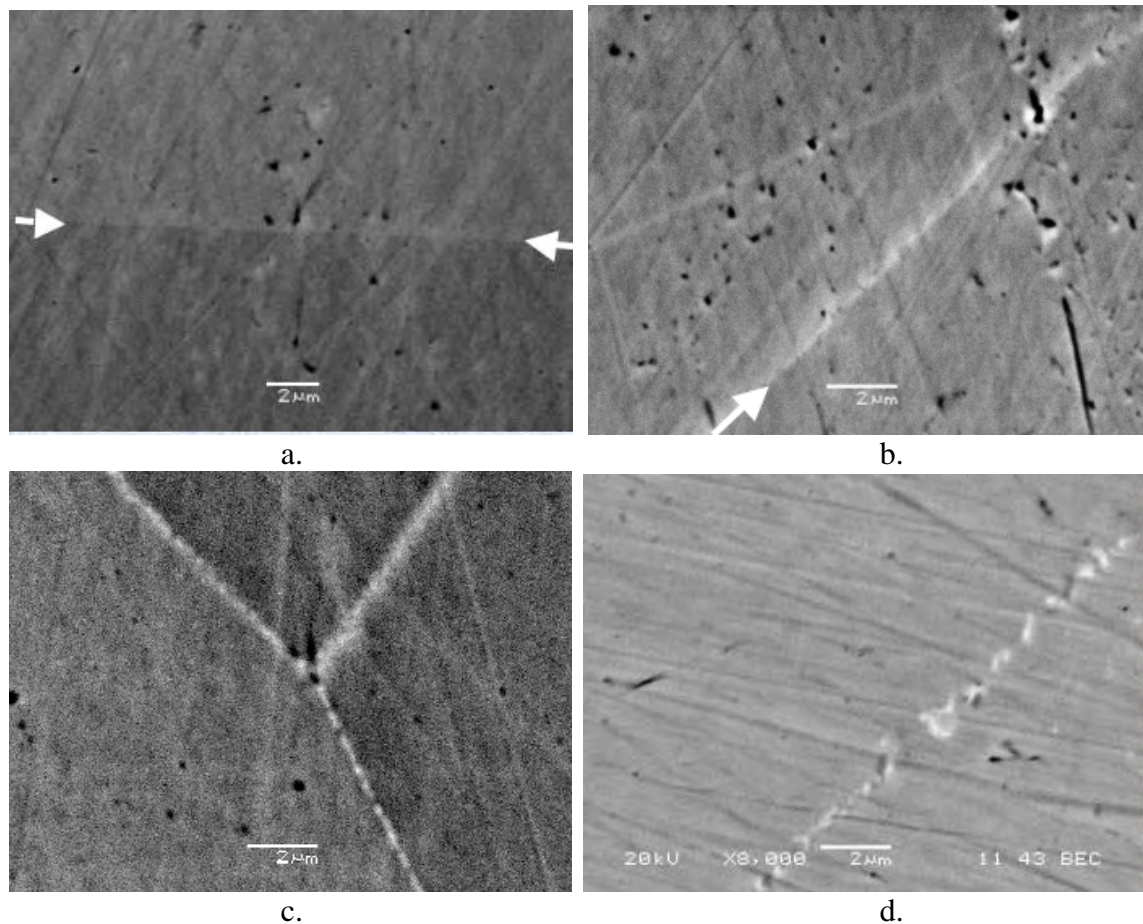


Figure 18: Polished SEM images of solution heat treated CN3MN that was subsequently heat treated at 872°C for a) 5 minutes; b) 15 minutes; c) 30 minutes; d) 1 hour. Arrows show the position of the grain boundary.

The contrast exhibited by the precipitates visible at longer times is consistent with phases higher in Cr and/or Mo than the surrounding matrix; the small size of the precipitates prevented any conclusions being drawn as to whether one or two different types of precipitates were present as discussed above.

Since grain boundary precipitation seemed to be playing a part in the observed embrittlement, linear percentages (distance along the grain boundary covered by precipitation / unit distance) quantifying the apparent grain boundary coverage were obtained from the images shown in Figure 18, and these values are given in Table V. It should be noted that all the measurements cited contain a great deal of uncertainty, especially at the shorter times of 5 and 15 minutes where low signal and small precipitate size require a considerable amount of judgment to be made as to whether a precipitate is, in fact, present. Given these difficulties, there is a good correspondence between measured linear coverage and the drop in impact strength seen in Figure 17, and this relationship is shown graphically in Figure 19.

Table V: Linear percentage of grain boundary coverage.

Annealing Time (Minutes)	Grain Boundary Coverage (Linear Percentage, %)
5	$\approx 0 \pm 8$
15	$\approx 33 \pm 8$
30	60 ± 5
60	65 ± 5

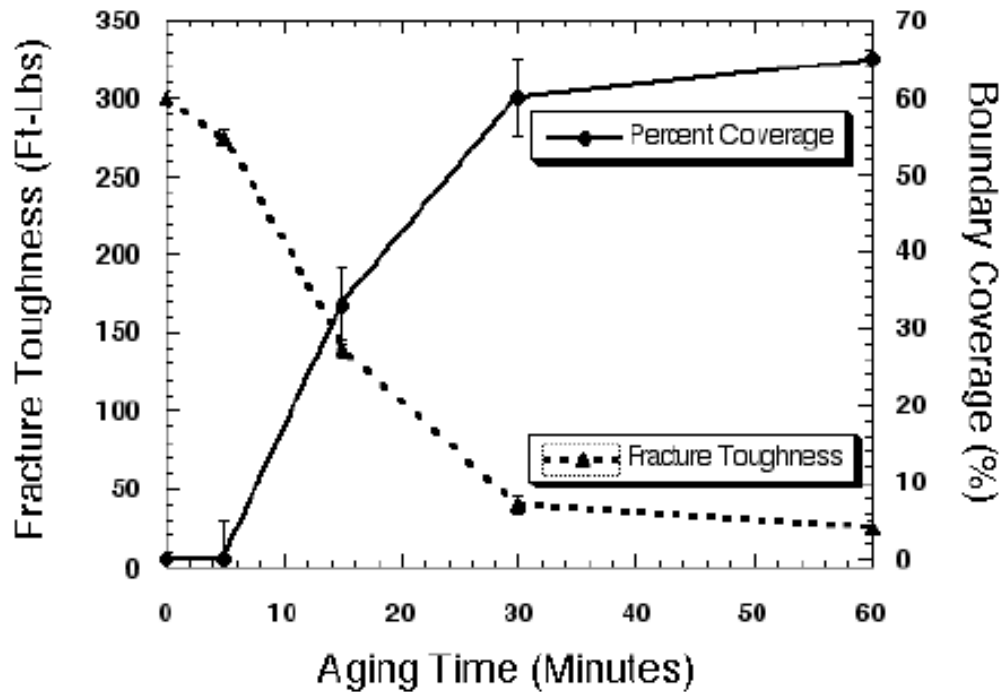


Figure 19: Correlation between drop in fracture toughness and increase of grain boundary precipitation coverage.

A final test of the hypothesis that grain boundary precipitation was responsible for the observed embrittlement was conducted by testing single crystal samples of CN3MN. Due to the limited size of the single crystal these tests involved small $\frac{1}{4}$ sized samples tested in the as SHT condition and embrittled and tested at room temperature and at -40°C . All of these samples withstood the applied force of the smaller Charpy Impact tester used, which should have been more than sufficient to cause fracture assuming embrittlement had occurred on the same scale seen for the polycrystalline samples. Images of these tested samples are shown in Figure 20.

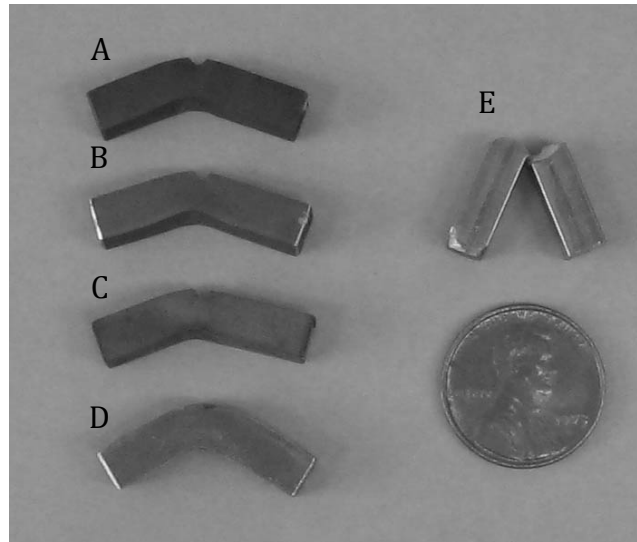
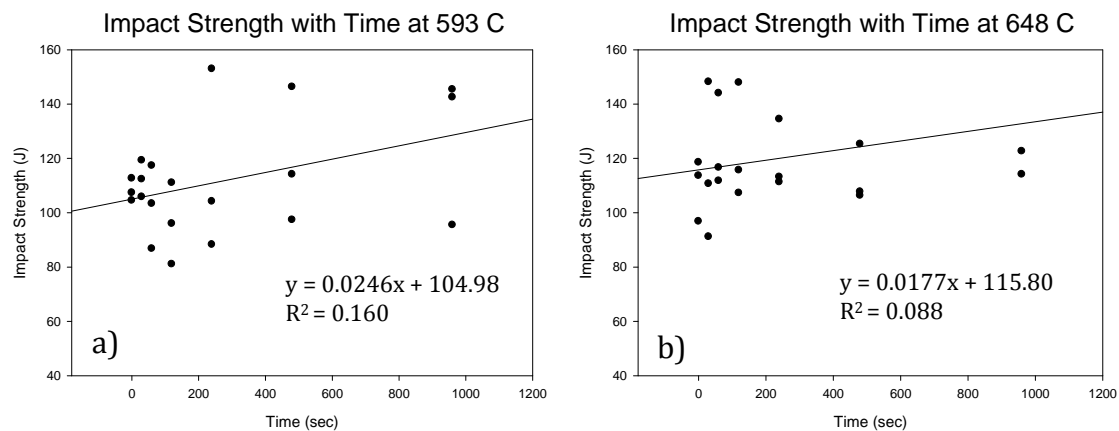


Figure 20: Single crystal impact samples. A: embrittled sample accidentally exposed to oxygen, room temperature test; B: solution heat treated, room temperature; C: embrittled, -40°C test; D: solution heat treated, -40°C (multiple strikes); E: A mild carbon steel sample fractured at room T for comparison.

4.3.2 Results: TTT Determination

Since fracture toughness was found to be extremely sensitive to minute amounts of grain boundary precipitation, a large test matrix of samples was developed for TTT diagram determination. Testing was conducted at room temperature and $\frac{1}{2}$ sized Charpy samples were used to ensure that all samples could be broken on a standard 300 ft/lb. Impact Tester. Samples were tested as SHT and at the times and temperatures given in Table II. The results are shown plotted in Figure 21. As a first approximation the data was described using a linear fit at each temperature. This is believed to be a reasonable assumption since a classic Avrami plot of percent transformation can be approximated as a linear decrease in the initial stages. The equation for the best-fit line and R^2 value are displayed on each graph.



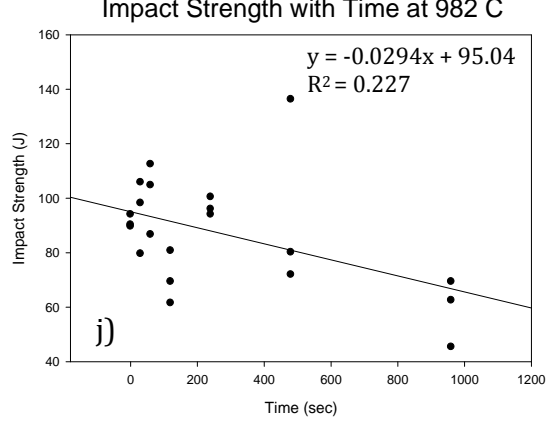
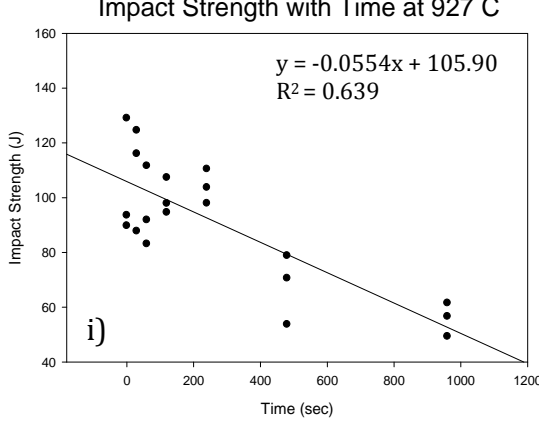
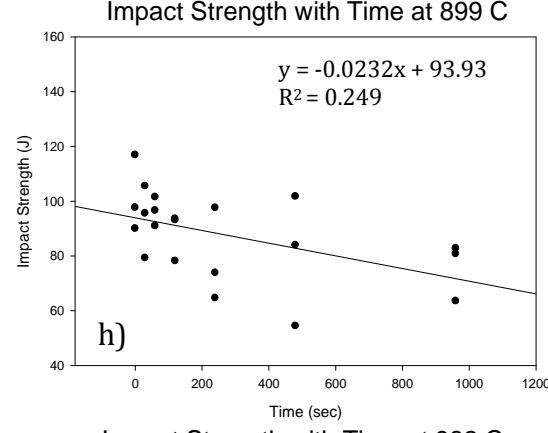
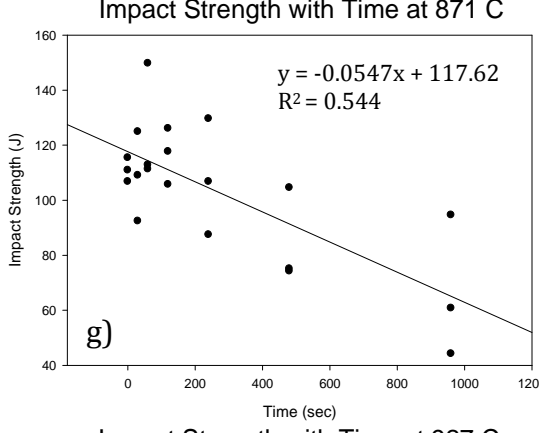
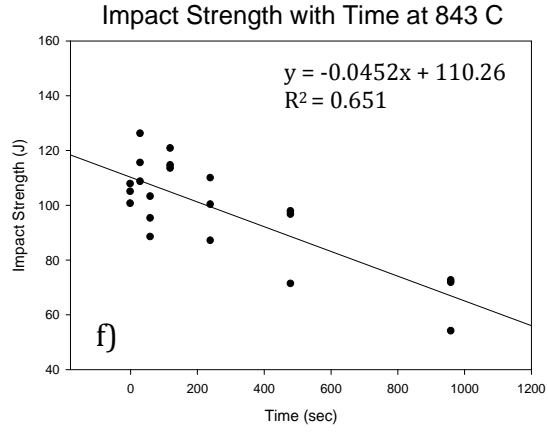
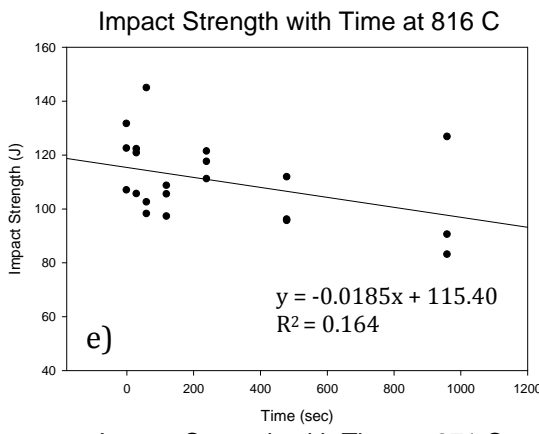
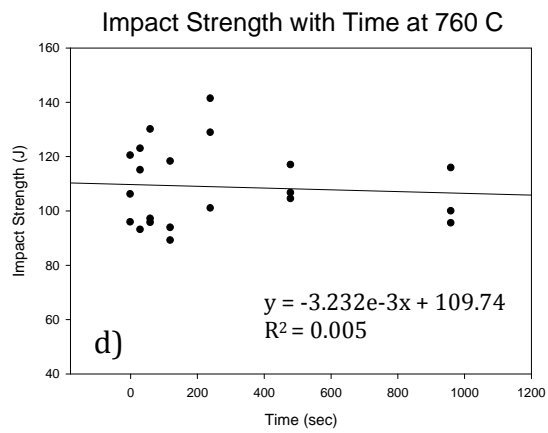
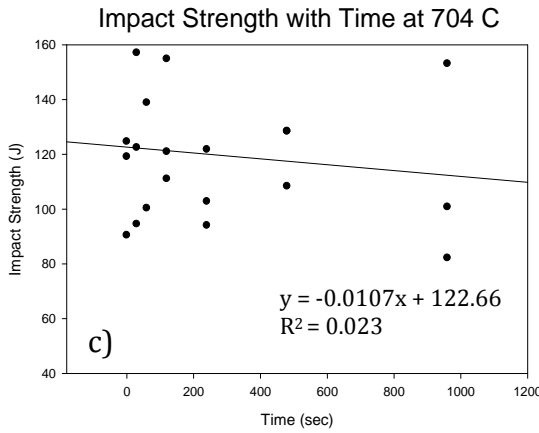


Figure 21: Impact Strength with respect to heat treatment time at a) 593 °C, b) 648 °C, c) 704 °C, d) 760 °C, e) 816 °C, f) 843 °C, g) 871 °C, h) 899 °C, i) 927 °C, and j) 982 °C.

At temperatures below 815 °C the impact strength shows little or no drop in toughness, with a slight toughening possibly occurring at the lowest temperatures. Starting at 815 °C the impact strength shows a steady decrease at temperatures up to the maximum tested of 982°C.

Chemical analysis using EDS was carried out on both bulk and brittle appearing areas, and the results are shown in Table VI. The nominal analysis was conducted on polished samples and represents an average of seven sampled regions. Seven regions from brittle surfaces were also sampled, the points considered being chosen to be as flat as possible to approximate as closely as possible the ideal of having a polished sample for quantitative analysis. Although the nature of the analysis (i.e. unpolished sample) limits the reliability of the quantitative numbers obtained from the brittle regions, it is clear that qualitatively the brittle surfaces contain a much higher percentage of Mo than the bulk.

Table VI: Qualitative analysis of weight percent composition of material and brittle fracture surfaces.

Element	Nominal	Brittle Surface
Si	1.61	2.95
Cr	21.94	22.67
Mn	0.89	0.92
Fe	48.29	45.58
Co	0.26	0.29
Ni	24.06	23.43
Cu	0.34	0.32
Mo	2.62	3.84

A transformation diagram for CN3MN was constructed using the linear best-fit trend lines shown in Figure 21. It should be noted that even samples listed at 0 seconds still have been subjected to thermal effects during the heating cycle since 0 represents the time taken to raise the sample to the desired set temperature followed by an immediate quench. Thus, the averaged value for material in the as-solution treated condition, i.e. 106.3 J, was used as the value for initial impact strength of the specimens before undergoing heat treatment. Observation of the data shows a large number of samples, particularly at the lower temperature heat treatments, have a higher value than this overall average. It is uncertain whether this indicates that a slight strengthening has occurred at the lower temperatures or whether this is just a result of scatter in the data. In either event, the averaged as-solution-heat-treated value was used for all subsequent calculations of percentage strength loss to maintain consistency when comparing the data.

Since the average fracture toughness of the solution heat treatment strength was 106.3 J, a loss of 10.6 J was assumed to be associated with a 10% loss in impact strength. The best-fit line for each specific heat treatment was then examined and the point at which a drop

of 10% from the solution heat treated was noted. The time associated with this loss, which is assumed to represent an average 10% over-all loss in solution heat treated strength, was then plotted on the transformation diagram. A sample calculation for a 10% loss at 843°C is shown below.

$$10\% \text{ Loss in Strength} = 106.3 J - 106.3 \times 0.1 = 95.67 J$$

Setting the Best Fit line for 843 °C equal to a 10% Loss in Strength

$$x = \text{time in seconds}$$

$$95.67 J = -0.0452x + 110.26$$

$$x = 323 \text{ seconds}$$

At 843°C a sample will have lost 10% of its solution heat treated strength in 323 seconds.

Following the example calculation above and solving for 10%, 20%, and 30% loss in impact strength for all temperatures, a transformation diagram can be obtained. This is done in Figure 22, which shows a transformation curve for embrittlement of CN3MN for the range 704° C to 982° C. Values for 593° C and 649° C were omitted due to the fact that they showed no noticeable loss in strength and, in fact, showed a slight increase in toughness. The rapid rate of embrittlement of CN3MN at temperatures above 843 °C is highlighted in an enlarged section of the TTT curve shown in Figure 23.

Examination of the transformation diagram shows that at both 899 °C and 982 °C the samples have undergone a 10% percent loss in strength by the time they reach the set temperature, due simply to the heating that occurs during the time required to reach temperature. This would imply that during that time the specimen was undergoing a transformation very rapidly.

There is a considerable amount of scatter in the data. This is accounted for by the fact that material from different foundries and different heats was used for this study. Although the heat compositions received with the keel bars all met specifications, as was noted above independent chemical analysis of the actual keel bars showed that the composition varied substantially. For example, one particular set of keel bars from Foundry E was found to be low in Mo content by about 1 wt%. Examination of the data obtained from the Charpy specimens machined from these keel bars found that they consistently showed lower initial fracture toughness. However, this was compensated for by a slower embrittlement rate, i.e., these samples held their strength as a function of time at temperature much better than did the remaining samples which were quite uniform in composition. These results would tend to support results discussed above as well as earlier studies that have shown high Mo phases to be the first intermetallics to form [14].

4.3.3 Discussion: CN3MN

Although not specifically studied by this project, it is clear that composition plays an important role in the kinetics of embrittlement. As this study was designed to represent conditions that exist within the industry, samples were taken from various heats provided by cooperating companies with no effort made to ensure that all samples contained exactly the same composition. However, earlier studies on duplex alloys have shown that small changes in composition can lead to dramatic effects in precipitation, and which intermetallic phase is the initial precipitate [11,17].

One effect of composition on the TTT curve determined in this study can be seen if the data from Foundry E is deleted from the analysis, where the amount of Mo in the keel bar (if not the overall heat as given by the provided analysis) was determined to be low. This is shown in Figure 24. Note that the nose shifts from around 927 °C to 899 °C and that the data holds a more consistent trend. This would indicate that Mo particularly is likely to promote early precipitation from solution. This is in agreement with the previous results discussed above. It also is in agreement with studies concerning the diffusion rates of Mo in highly alloyed steels and that extended times and high temperatures must be used in order to obtain a homogenous structure [14-16].

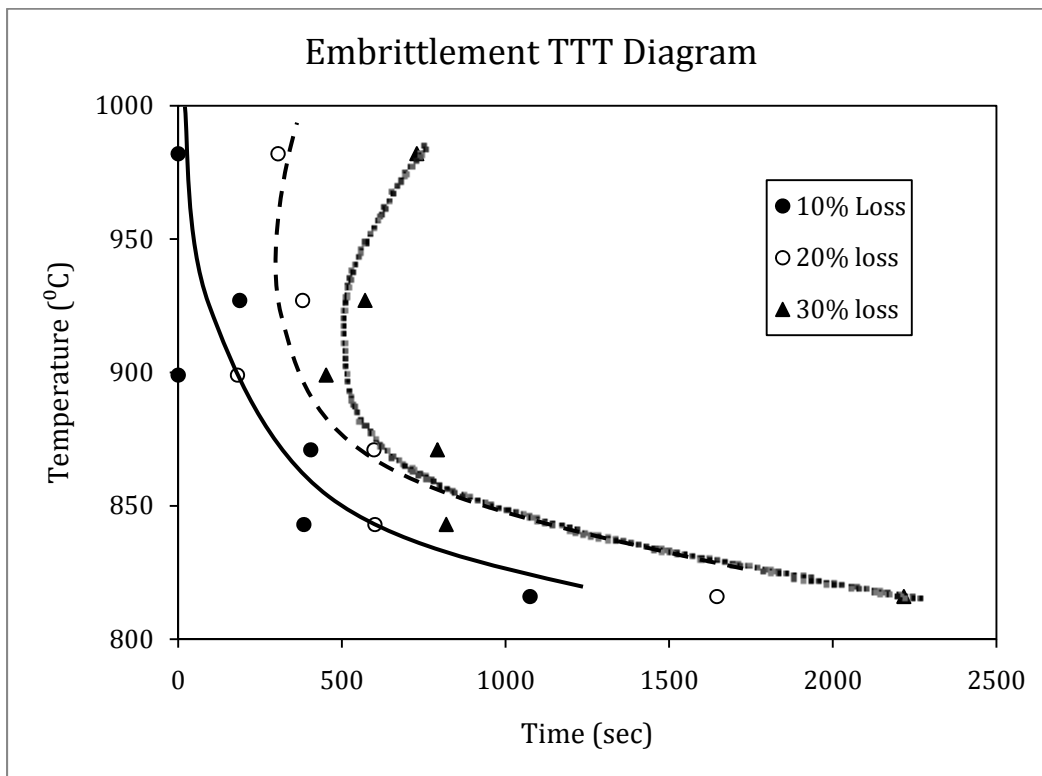


Figure 24: Embrittlement TTT Diagram with Foundry E removed from the calculation.

5. Benefits Assessment

The main benefits of this research has been in identifying the scientific reasons why castings may fail due to poor fracture toughness and / or poor corrosion resistance and providing guidelines to follow to avoid such failures. By identifying the reasons for failure, namely, intermetallic formation on grain boundaries and the time / temperature regimes under which harmful intermetallics can occur, companies can now use advanced heat-flow software to determine whether any particular casting, or part of a large casting, will be subject to cooling conditions that would lead to precipitate formation. The experimental results obtained relating specific intermetallic formation to composition can also provide guidance in determining solution heat treatment times and temperatures to improve casting quality. These results can produce significant energy savings in two ways. Firstly, by reducing the number castings that need to be scrapped savings are generated by eliminating costs associated with completely remaking a casting. Secondly, by identifying the time / temperature ranges at which precipitation is a problem, heat treatment schedules can be more efficiently planned and executed.

This development of high alloy steel CCT diagrams was predicted to result in an average energy savings of 0.05 trillion BTU's/year over a 10 year period (with full funding). With 65% of the proposed funding, current (2011) annual energy saving estimates, based on initial dissemination to the casting industry in 2011 and market penetration of 97% by 2020, is 0.14 trillion BTU's/year.

The reduction of scrap and improvement in casting yield will also result in a reduction of environmental emissions associated with the melting and pouring of the steel. The average annual estimate of CO₂ reduction per year through 2020 is 0.003 Million Metric Tons of Carbon Equivalent (MM TCE).

6. Commercialization

As this work consists of basic research there is no formal commercialization. Dissemination of the results will be made to the US steel casting industry through presentations, industry review committees, technical societies associated with steel casting such as the Steel Founders Society of America (SFSA), and publication of data in trade and refereed journals. This wide-spread dissemination of the research results will allow industries to easily incorporate the data into their existing operation plans. By careful analysis of the data, steel foundries can determine what changes are most suitable for their particular operations in a rapid and efficient manner.

7. Accomplishments

The major project accomplishment is in providing for the first time accurate and easily accessible data concerning the phase transformations present in specific cast alloys CN3MN and CK3McuN as a function of time and temperature. These results can

produce significant energy savings by 1) reducing the number of scraped / reworked castings; and 2) utilizing more efficient heat treatment schedules.

Other tangible accomplishments are summarized as follow:

One M.S. degree was granted to Mr. Nate Phillips. Mr. Phillips is now employed at the Caterpillar Technical Center in Mossville, Illinois, a company that is a large user of steel castings.

Two undergraduate students worked on this project, Mr. Chris Muller, who currently is employed by 2H Offshore Inc., and Mr. Barry King, currently employed by MetalTek. MetalTek is a maker of high alloy castings while 2H Offshore is a user of high quality corrosion resistant castings.

Three papers have either been published or accepted for publication in refereed international journals.

Four papers were published in the proceedings of meetings of the Steel Founders Society of America. This reflects the fact that four invited presentations were also given at these conferences.

Two invited presentations concerning research developments were given to the High Alloy Research Committee, a working group of SFSA.

8. Conclusions

8.1 Research Conclusions:

Backscattered electron SEM images of the superaustenitic alloys CK3McuN and CN3MN revealed an obvious contrast between two intermetallics and the austenitic matrix. Phase identification using TEM coupled with WDS measurements revealed BCT- σ and HCP- Laves phases, which formed at all temperatures studied in both alloys.

The transformation kinetics of both CN3MN and CK3McuN were extremely sluggish. Equilibrium conditions were not reached in either alloy after 2040 hour at 700 to 900°C. The transformations occurred fastest at 900°C, indicating the maximum transformation rate could be at temperatures higher than 900°C.

Precipitation in CK3McuN begins with the formation of high-Cr plate-like σ along the interdendritic boundaries and near voids. Shortly thereafter, the needle-like Laves formed intradendritically around the σ . Laves continued to nucleate within the dendrites and σ shortly followed.

Macroseggregation of Mo was seen in the cast and solution treated samples of CN3MN. Laves formed only in high-Mo interdendritic regions, while higher σ amounts were found in the intradendritic regions than in interdendritic regions. Laves phase subsequently dissolved, indicating metastability. The stable σ phase continued to grow at the maximum heat treatment time of 2040 hours at all temperatures in CN3MN and at 700 and 800°C in CK3McuN. The σ at 900°C in CK3McuN stabilized at approximately 12 vol. %.

Intradendritic nucleation and growth of σ was much slower than the Laves, possibly due to a crystallographic orientation relationship between the HCP- Laves and FCC- σ . The nucleation and growth rate of Laves in CN3MN was much faster at 800 and 900°C than in CK3McuN. The nucleation rate of σ was also much faster in CN3MN; however, the growth rate was slower. The slow growth rate can be attributed to the segregation of Mo in the interdendritic regions, which made the formation of Laves preferential. The macroseggregation of Mo seen in CN3MN could have been avoided if the as-cast bars were solution heat treated at temperatures and times that allowed for complete dissolution of Mo.

Number density and volume percent studies indicated that growth and coarsening of σ occur simultaneously in both alloys. This phenomenon is assumed to be a result of local compositional differences.

Charpy impact tests run on samples solution heat treated then annealed showed fracture toughness dropped drastically after the improper heat treatment of 872° C for 1 hour, the failure mode being intergranular cleavage. The noted embrittlement occurred well before any significant amounts of precipitation had occurred in the sample as predicted by the initial equilibrium studies. Characterization of the fracture surfaces using SEM and a combination of X-ray EDS and Auger spectroscopies revealed extremely small precipitates on the grain boundaries that are enriched in Mo and Cr. Although the small size scale of the precipitates prevented conclusive identification, they are assumed to be either sigma or Laves phase, the intermetallics observed to first precipitate in CN3MN.

Further Charpy studies over a larger temperature range showed CN3MN undergoes a rapid loss in impact strength when heat treated in the range 843 °C to 982 °C. The loss can be as great as 30% percent of the as-solution heat treated value for times as short as 960 seconds, with a 10% loss being seen almost immediately upon heating to these temperatures. The nose of the TTT curve begins near 899 °C. Fracture surfaces of CN3MN with low impact strength all displayed high levels of brittle fracture and surface compositions high in Mo and Si, indicating that formation of a Mo-rich precipitate on grain boundaries is the most likely reason for the embrittlement. This is supported by previous studies in the duplex alloys and by the observation that data keel bars that were found to be somewhat low in Mo had lower initial strengths but were more resistant to embrittlement than those with higher Mo additions.

8.2 General Project Conclusions:

Comments made by company representatives at technical meetings and in private discussions indicate there is a great need for studies of this type. In order to remain competitive, US companies are being increasingly forced to operate as efficiently as possible in order to off-set lower labor costs from off-shore sources. Basic studies of this type provide the information necessary for them to do so.

Greater accomplishments can be obtained by a combination of more precise phase characterization using TEM to identify initial precipitation events, design of experiments to study the effect of alloying on the first phases to form, and computational modeling using packages such as ThermoCalc to predict the effects on phase formation as a function of alloying content. Although Thermo-Calc is often inaccurate in predicting final amounts and temperatures in these highly alloyed systems, the trends of precipitation as predicted are generally true and could be used to tailor alloying additions to produce alloys more resistant to rapid embrittlement.

9. Recommendations

In order to complete the work started in this project it is recommended that a final study be undertaken employing TEM to completely characterize the nature of the intermetallics that form in the initial stages of precipitation. Experiments could be conducted in-situ in the TEM to determine the composition and structure of the initial precipitation events occurring on grain boundaries. Based on these results experiments could run, in conjunction with computer thermodynamic simulations, to determine which alloying additions are most critical in causing precipitation to occur. Advanced alloys could then be developed where these elements are either tightly controlled to reduce precipitation of additional alloying is used to mitigate the harmful effects.

10. References

1. Stefan Heino, "Role of Mo and W during Sensitization of Superaustenitic Stainless Steel –Crystallography and Composition of Precipitates," *Metallurgical and Materials Transactions*, 31A (2000), 1893-2904
2. S. Heino, M. Knutson-Wedel and B Karlsson, "Precipitation in High Nitrogen Superaustenitic Stainless Steel," *Trans Tech Publications Ltd.*, 2005
3. M. Svoboda, A. Kroupa, J. Soousek, J. Vrest'al, and P. Miodownik, "Phase Changes in Superaustenitic steels after long-term annealing," *Z Metallk*, 95 (2004), 1025-1030.
4. T-H. Lee, S-J Kim, and Y-C, Jung, "Crystallographic Details of Precipitates in Fe-22Cr-21Ni-6Mo-(N) Superaustenitic Stainless Steels Aged at 900°C," *Metallurgical and Metals Transactions*, 31A (2000), 1713-1723.
5. S. Heino, M. Knutson-Wedel, B. Karlsson, *Materials Science Forum*, 318-320 (1999), 143-148

6. Y.-J. Kim, L. S. Chumbley, B. Gleeson, "Development of Isothermal Transformation Diagrams for Sigma-Phase Formation in Cast Duplex Stainless Steels," Proceedings, *Steel Founders' Society of America 2003 T&O Conference*, 2003.
7. N. Saunders, A. P. Miodownik, "CALPHAD (Calculation of Phase Diagrams), A Comprehensive Guide", Pergamon Materials Series, Oxford, UK, Elsevier, Vol.1, 1998.
8. C. W. Kovach, "High-Performance Stainless Steels", Nickel Institute, Toronto, Ontario, Canada, 2000.
9. N. Phillips, L.S. Chumbley, B. Gleeson, and O. Ugurlu. "Determination of Phase Transformations in Cast Superaustenitic Stainless Steels." Technical and Operating Conference. Chicago, IL: Steel Founders Society of America, 2006.
10. M. Blair. "Special Report Number 31" Crystal Lake, IL: Steel Founders Society of America, (2001):1-52
11. Y-J Kim, L. S. Chumbley, and B. Gleeson. "Continuous Cooling Transformation in Cast Duplex Stainless Steels CD3MN and CD3MWCuN." Journal of Materials Engineering and Performance (2008):234-239
12. Lundin, C. D., and V. Hariharan. *Behavior of Duplex Stainless Steel Castings*. Volumes (1-5). U.S. Department of Energy, 2005.
13. C. Muller, and L. S. Chumbley. "Fracture Toughness of Heat Treated Superaustenitic Stainless Steels." Journal of Materials Engineering and Performance (2009): 714-720.
14. J. D. Farren and J. N. Dupont. "Heat Treatment of High Alloy Stainless Steel Castings". Technical and Operating Conference. Chicago, IL: Steel Founders Society of America, 2006.
15. S. W. Banovic, J. N. DuPont, A. R. Marder. "Dilution and Microsegregation in Dissimilar Metal Welds between Super Austenitic Stainless Steel and Nickel Based Alloys." Science and Technology of Welding and Joining (2002): 374-383.
16. T. D. Anderson, J. N. Dupont, A.R. Marder, and M. J. Perricone. "The Influence of Molybdenum on Stainless Steel Weld Microstructures." Welding Journal (2007): 281-292.
17. Y-J Kim, O. Ugurlu, C. Jiang, B. Gleeson, and L. S. Chumbley. "Microstructural Evolution of Secondary Phases in the Cast Duplex Stainless Steels CD3MN and CD3MWCuN." Metallurgical and Materials Transactions (2007): 203-211.

11. Appendix A

Energy Savings Benefits Analysis

The development of Continuous Cooling Transformation (CCT) diagrams for steel castings specifically establishes needed data for steel casting that have been identified, as near term and mid-term materials technology research needs to improve the quality of castings (preventing intermetallic precipitates such as sigma (σ) and Laves that can form during casting or exposure to high-temperature processing, which degrade the corrosion and mechanical properties of the material).

Direct economic benefits from the utilization of CCT diagrams for heat treatment qualification procedures accrue from the reduced requirements for re-heat treatment and shutdown avoidance. Energy savings are detailed below:

The steel castings sold = 1,040,000 tons/ Yr (in 2000, source: U.S. Dept. of Commerce)

Castings requires reheat treatment = 15% = 156,000 tons / Yr

Energy used in reheat treatment = $3.04 * 10^6$ BTUs / Ton

Recleaning = $0.34 * 10^6$ BTUs / Ton

Total = $3.38 * 10^6$ BTUs / Ton

Total energy used in reheat process (energy saved) = $3.38 * 10^6$ Btu per ton * 156,000 tons/yr

= $5.27 * 10^{11}$ BTUs / Yr = $0.527 * 10^{12}$ BTUs / Yr (at 100% penetration)

A market growth of 1.7% was assumed for steel castings (Source: AFS Metalcasting Forecast & Trends 2002, Oct 2001). Introduction into industry is 2011 and a 97% penetration (of the 15% subset market of castings requiring reheat treatment) was assumed by 2020. Annual energy saving estimates, based on initial dissemination to the casting industry in 2011 and market penetration of 97% by 2020, is 0.14 trillion BTU's/year.

Sources:

CMC rules of thumb website (http://cmc.aticorp.org/Energy_metrics.html), industry energy estimates. U.S. Department of Commerce, U.S. Census